Supporting information

Unraveling the Sodium Storage Mechanism in a Redox-Active Covalent Organic Framework Cathode for Na-Ion Batteries

Jonathan Caroni,[a,⊥] Asia Patriarchi,[b,⊥] Jon Otegi,[c] Leonardo Sbrascini [d], Hegoi Manzano,[c] Javier Carrasco,[e,f] Manuel Souto [a,g*], Miguel Ángel Muñoz-Márquez [b,d,h,*]

⊥ All authors contributed equally.

* Corresponding author: miguel.munoz@inl.int, manuel.souto.salom@usc.es

[a] J. Caroni, Dr. M. Souto
CiQUS, Centro Singular de Investigación en Química Bioloxica e Materiais Moleculares, Departamento de Química-Física,
Universidade de Santiago de Compostela
15782, Santiago de Compostela, Spain

E-mail: manuel.souto.salom@usc.es

[b] A. Patriarchi, Dr. M. Á. Muñoz-Márquez
School of Science and Technology; Chemistry division
University of Camerino, via Madonna delle Carceri- ChIP
62032 Camerino (MC), Italy
E-mail: miguel.munoz@inl.int

[c] J. Otegi, Dr. H. Manzano
Department of Physics, University of the Basque Country (UPV/EHU)
Sarriena auzoa, z.g., 48940 Leioa, Spain

[d] Dr. L. Sbrascini, Dr. M. Á. Muñoz-Márquez
International Iberian Nanotechnology Laboratory
Av. Mestre José Veiga, s/n
4715-330 Braga, Portugal

[e] J. Carrasco
Centre for Cooperative Research on Alternative Energies (CIC Energigune), Basque Research and Technology Alliance (BRTA)
Araba Technology Park, Albert Einstein 48, 01510 Vitoria-Gasteiz, Spain

[f] Dr. J. Carrasco
IKERBASQUE, Basque Foundation for Science
Plaza Euskadi 5, 48009 Bilbao, Spain

[g] Dr. M. Souto

Oportunius, Galician Innovation Agency (GAIN),

15702 Santiago de Compostela, Spain

[h] Dr. M. Á. Muñoz-Márquez

National Reference Center for Electrochemical Energy Storage (GISEL)

Via Giusti 9, 50121Firenze (FI), Italy.

Experimental Procedures

1.1 Reagents

2,6-Diaminoanthraquinone and anthracene-2,6-diamine were sourced from BLD PHARMATECH, 1,3,5-tris (4-formylphenyl) benzene (TFP) was purchased from ET Co,Ltd. Acetic acid, N,N−Dimethylacetamide (DMAc) and mesitylene solvents were obtained from Fisher Scientific and TCI chemicals. 1-methyl-2-pyrrolidone NMP (Sigma-Aldrich), conductive carbon Super C65 (Timcal), polyvinylidene fluoride (PVDF SOLEF 5130, Solvay), diethylene glycol dimethyl ether (DEGDME, Anhydrous, Sigma-Aldrich), sodium hexafluorophosphate $NaPF_6$ (98%, Thermo Fisher) were used as received.

1.2 Synthetic procedure of DAAQ TFP COF

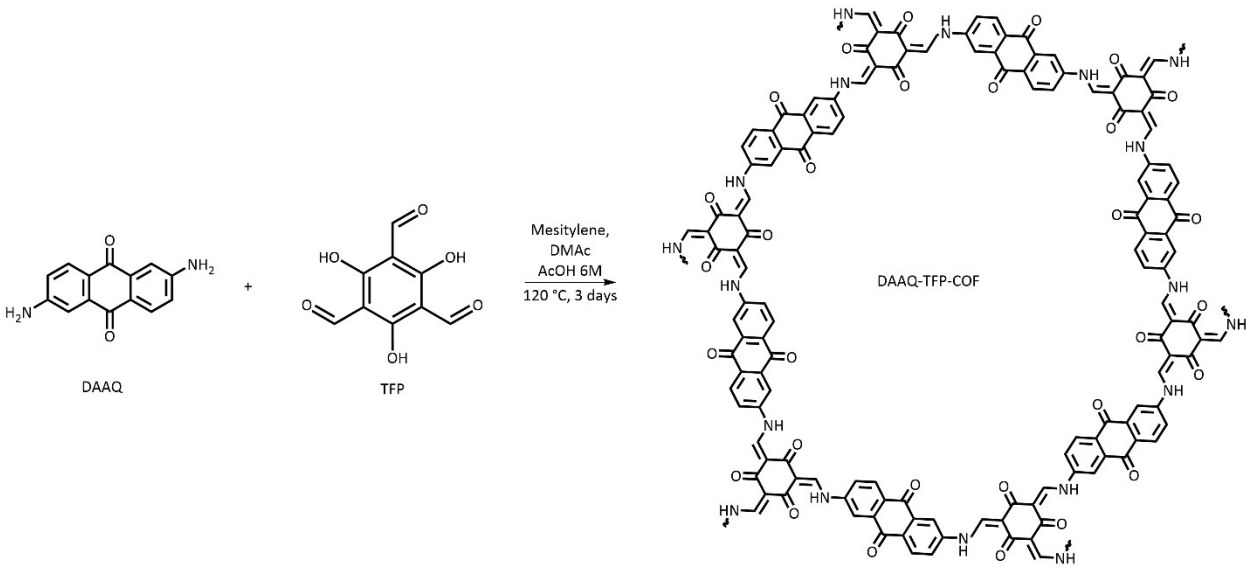

The material was synthesized following a reported procedure.[1] A 10 mL Pyrex tube was loaded with 20 mg (0.095 mmol) of 1,3,5-tris(4-formylphenyl)benzene (TFP) and 34 mg (0.142 mmol) of 2,6-diaminoanthraquinone (DAAQ) in a solvent mixture of 0.9 mL DMAc and 0.3 mL mesitylene. The resulting suspension was sonicated for 30 seconds at room temperature before adding 50 µL of 6 M acetic acid. The tube underwent three freeze-pump-thaw cycles, was sealed, and heated at 120 °C for 3 days. The resulting powder was filtered, washed thoroughly with DMF and acetone, and dried under vacuum at 180 °C for 24 hours.

1.3 Synthetic procedure of Da TFP COF

A 10 mL Pyrex tube was loaded with 42 mg (0.2 mmol) of 1,3,5-tris(4-formylphenyl)benzene (TFP) and 62.4 mg (0.3 mmol) of 2,6-diaminoanthracene (Da) in a solvent mixture of 1 mL dioxane and 1 mL mesitylene. To the resulting suspension was added 200 µL of 8 M acetic acid and then sonicated for 15 minutes at room temperature. The tube underwent three freeze-pump-thaw cycles, was sealed, and heated at 120 °C for 3 days. The resulting powder was centrifugated and washed thoroughly with dimethylacetamide (N,N- DMA), water and Acetone and dried under vacuum at 150 °C for 24 hours. [2]

1.4 Electrode manufacturing

The cathode slurry was prepared by dispersing 60 wt% active material, 30 wt% conductive carbon, and 10 wt% polyvinylidene fluoride in N-methyl-2-pyrrolidone under magnetic stirring for 6–8 hours to achieve a homogeneous mixture. A 30 wt.% conductive-carbon content is relatively high compared with inorganic cathodes, however, the intrinsically low electronic conductivity of DAAQ-TFP COF necessitates a larger conductive additive fraction to establish a percolating network and enable efficient charge transport. [1,3,4] The resulting viscous slurry was then cast onto 20 μm-thick aluminum foil using a doctor blade, setting a coating thickness of approximately 100 μm (mass loading 1-1.5 mg cm^{-2} /0.151- 0.226 mAh cm^{-2}). The laminate was initially dried under vacuum to evaporate the solvent, followed by electrode punching. To eliminate residual solvent traces and moisture, the electrodes underwent further drying in a Büchi oven at 120°C for 4 hours. Finally, the cathodes were transferred to an argon-filled glovebox (MBraun, O_2 and H_2O levels < 1 ppm) for subsequent cell assembly.

Six electrodes with varying thicknesses reduction (from 0 to 55% volume reduction) were obtained by calendaring the laminate.

1.5 Characterization techniques

Powder X-Ray diffraction (PXRD) pattern of the sample was recorded at room temperature with a Bragg-Brentano geometry on a "Bruker D8 Advance" X-ray diffractometer (40 kV, 40 mA, θ/θ configuration). The diffractometer was equipped with a sealed Cu X-ray tube (λ Cu $K\alpha_1$ = 1.5406 Å) and a LYNXEYE detector. The diffractograms of the powder were obtained in the angular range of 3 to 40 θ with a step size of 0.02° (2θ) at 1s per step. The samples were placed on a Si (511) oriented crystal base to avoid background noise caused by a traditional glass support. The electrodes diffractograms were obtained in the angular range of 2 to 30θ with a step size of 0.04° (2θ) at 6s per step. The ex-situ air-sensitive samples were measured with a specific airtight specimen holder with dome-type, X-ray transparent cap with Si (511) low-background base. These measurements were taken with an incident beam Göbel mirror for the parallel beam geometry to minimize the effect of sample displacement.

Small-Angle X-ray Scattering (SAXS) and Wide-Angle X-ray Scattering (WAXS) measurements were performed using an Anton Paar SAXSpoint 5.0 beamline equipped with a Primux 100 micro–Cu X-ray source (λ = 0.154 nm), multilayer mirror optics (ASTIX 2D), and two 2D EIGER2 R detectors: a 1M detector for SAXS and a 500K detector for WAXS. The samples were measured at two detector distances, 1621 mm and 350 mm, covering a q-range of 0.004 to 0.19 $Å^{-1}$ for SAXS and 0.18 to 2.3 $Å^{-1}$ for WAXS. For each sample, 50 images were recorded with an acquisition time of 15 s per scan. Silver behenate was used for instrument q-scale calibration.

Pawley refinement and fittings through pseudo-Voigt profile functions on the experimental PXRD and WAXS patterns were performed using X'Pert High Score software. Simulated eclipsed AA stacked structural model of DAAQ-TFP COF was obtained through the creation of a model with pyCOFBuilder. [5]

A shape-independent mass-surface fractal fitting, well-suited for the complex fractal system of the electrode composed by COF, PVDF, and carbon black, was performed on the SAXS data collected from both the pristine and calendered electrodes using SasView 6.0.0 software (www.sasview.org/).[6,7]

Gas adsorption measurements were recorded on a Micromeritics 3Flex apparatus. The sample was degassed overnight at 100ºC and 10^{-6} Torr prior to analysis. BET surface values were calculated from the N_2 isotherms using BETSI1 and pore size distributions were obtained using the non-local density functional theory (NLDFT) method.[8]

Thermogravimetric analysis (TGA) of DAAQ-TFP was conducted employing a TA Instruments Q5000 IR thermobalance. The TGA measurements involved a general heating profile ranging from 25 to 800 °C, with a heating rate of 5°C min^{-1} under an N_2 atmosphere using a gas flow rate of 25 mL min^{-1}.

Fourier transform infrared spectroscopy (FTIR) measurements were conducted employing a PerkinElmer Spectrum Two spectrometer equipped with Attenuated Total Reflection (ATR) capability. The dried powder was positioned on the ATR window for analysis within the wavenumber range of 400 to 4000 cm^{-1}.

Scanning Electron Microscopy (SEM) (Zeiss Sigma 300 FM) was employed to investigate the morphology of the COF and any structural modifications in the electrodes after cycling or calendaring. Additionally, Energy Dispersive X-ray Spectroscopy (EDX) was used to analyze the chemical composition of the samples and confirm the absence of impurities.

Transmission electron microscopy (TEM) images were collected using a JEOL JEM-2100-HT TEM operating at 200 kV and equipped with a fast-readout "OneView" 4k × 4k CCD camera that operates at 25 fps (300 fps with 512 × 512 pixel). The sample was prepared by dropping a diluted suspension of the material onto a carbon-coated Cu grid (CF300-Cu-UL, Electron Microscopy Sciences), followed by evaporation of the solvent. After drying, the grids were left under vacuum for 3 hours before analysis under the microscope.

1.6 Electrochemical characterization

The electrochemical characterization of the materials was performed using two-electrode CR2032 coin cells. Sodium metal (Ø = 9 mm) was used as the counter electrode, while two Celgard 2400 disks (Ø = 16 mm) served as separators. 1 M $NaPF_6$ in DEGDME was selected as the electrolyte. Cyclic voltammetry (CV) was conducted within a 1.0–3.0 V potential range at scan rates ranging from 0.1 to 5.0 mV s^{-1}. Additionally, galvanostatic cycling with potential limitation (GCPL) was carried out at a C-rate of 2C (1C = 151 mAh g^{-1}). Rate capability tests were performed at different current rates (C/10, C/5, C/2, 1C, and 2C), with each rate applied for five cycles, followed by a return to the slowest rate (C/10) within the 1.0–3.0 V voltage window. A three-electrode ECC PAT-Core EL-Cell with pre-assembled Na metal ring reference and Whatman GF/D glass fiber separator (d = 20 mm) was used for the potentio electrochemical impedance spectroscopy (PEIS) measurements, employing sodium metal (d = 14 mm) as the counter electrode. Impedance spectroscopy measurements were performed during the 10^{th} cycle (C/5 current rate), at selected bias potentials. Specifically, the regions 1.4 V < E < 1.6 V and 1.8 V < E < 2.0 V have been chosen during desodiation, while the regions 1.9 V > E > 1.7 V and 1.5 V > E > 1.3 V have been chosen during sodiation. A sinusoidal perturbation of $\Delta E = \pm 10$ mV was applied over the frequency range 100 mHz < f < 199 kHz in single-sine mode, with 10 points per decade and logarithmic spacing. A 2-hour potentiostatic step was applied prior to each impedance measurement, to allow the cell to reach equilibrium conditions. The total harmonic distortion (THD I%) and the non-stationarity distortion (NSD I%) indicators have been monitored during the PEIS experiment, to ensure that all responses satisfy linearity and stationarity conditions (frequency range 100 mHz < f < 10 kHz). The calculation of the distribution of relaxation times (DRT) and distribution of differential capacitance (DDC) functions was performed after subtraction of the low-frequency diffusive contribution from the complex Nyquist impedance and complex Cole-Cole capacitance plots, respectively. The subtraction was performed after fitting the AC dispersions to an Equivalent Circuit Model (ECM), through the NLLS method.[9,10] The optimization of the λ-factor for the DRT/DDC analyses was performed by calculating the sum of squared residuals (SSR) vs. λ plot, assuming a Gaussian distribution, according to Tikhonov regularization.[11,12] Both the fitting procedure and the calculation of the DRT/DDC functions were performed by using the software *RelaxIS3*.

All cells were assembled in an argon-filled glovebox with oxygen and moisture levels maintained below 1 ppm. Electrochemical measurements were conducted using a VMP-3 multichannel workstation with an integrated frequency response analyzer from Bio-Logic. All potential values are referred to the Na^+/Na redox couple ($E° = -2.71$ V vs. RHE).

1.7 Ex-situ measurements

For ex-situ SEM analysis, electrodes were recovered under an argon atmosphere to prevent air exposure, rinsed with glyme to remove residual electrolyte, and subsequently examined.

Ex-situ X-ray diffraction (XRD) measurements were performed on the pristine electrode, postmortem electrode, and at various states of charge. Prior to analysis, the postmortem, sodiated, and desodiated electrodes were washed with glyme to eliminate electrolyte residues. The samples were then sealed in an airtight specimen holder with a dome-type, X-ray-transparent cap and a low-background Si (511) base before analysis.

To examine the nature of the cathode-electrolyte interphase (CEI) formed with different electrolytes, the pristine electrode was analyzed alongside electrodes at open-circuit voltage, after SEI formation, and following the first stripping and plating cycle. The study included three electrolyte compositions: 1 M $NaPF_6$, 0.5 M $NaBF_4$, and a $NaPF_6$/$NaBF_4$ mixture (3:1 v/v) in DEGDME. Before analysis, all electrodes were rinsed in glyme for 30 seconds to remove residual electrolyte.

Ex situ SAXS and WAXS analysis were performed on washed electrodes with the same procedure described above.

1.8 Computational details

1.8.1 Density Functional Theory (DFT)

First-principle calculations were performed using the SIESTA package, based on density functional theory (DFT).[13,14] The generalized gradient approximation (GGA) with the Perdew-Burke-Ernzerhof (PBE) exchange-correlation functional was used, along with the Grimme DFT-D3 dispersion correction to account for van der Waals interactions between COF layers.[15,16] The pseudo-atomic orbital were expanded using a double-ζ polarized basis set. The cutoffs were set to 500.0 Ry for the real-space mesh and 25 Bohr for the *k*-grid. Geometry optimizations were carried out using the conjugate gradients method, with a force tolerance of 0.05 eV/Å.

Following the literature, the binding energy of the sodiated stage *x* was calculated using the following formula:[17]

$$\Delta E_x = E_{COF-xNa} - \left(E_{COF-(x-1)Na} + E_{Na}\right)$$

where *x* is the number of sodium atoms in each configuration, $E_{COF\text{-}xNa}$ and $E_{COF\text{-}(x\text{-}1)Na}$ are the total energies of the COF structure with *x* and *x*-1 sodium atoms respectively, and E_{Na} is the energy per atom of bulk metallic sodium. For the calculation of the potential with respect to the metal electrode at sodiation stage *x*, we used the following formula:[18]

$$U_x = -\frac{1}{xnF}\left[E_{COF-xNa} - \left(E_{COF} + E_{Na}\right)\right]$$

where $E_{COF\text{-}xNa}$ and E_{Na} are defined above, E_{COF} is the total energy of the pristine COF, *x* is the number of sodium atoms, *n* is the charge of the sodium cation (assumed to be +1), and *F* is the Faraday constant.

1.8.2 Molecular dynamics (MD)

MD simulation details were based on our previous work, which we summarize here.[19]

To realistically model electrolyte-filled COF channels, we constructed our MD box based on the experimentally resolved unit cell of DAAQ-TFP-COF. The hexagonal unit cell was transformed into an orthorhombic configuration and replicated to generate a 2x2x15 supercell. The resulting system, consisting of 180 DAAQ and 120 TFP units, features four hexagonal channels aligned along the *z*-axis, serving as conduits for ion transport. These channels were then filled with LiTFSI@DEGDME electrolyte using the PACKMOL package.[20] Assuming the electrolyte occupies the available pore volume, and to replicate an experimental salt concentration of 1 M, we inserted 13 ion pairs and 80 solvent molecules per channel. The final simulation box comprised a total of 14576 atoms.

We performed all MD simulations using the LAMMPS package.[21] Intramolecular interactions were modeled using the all-atom optimized potentials for liquid simulations (OPLS-AA) force field.[22] Force field parameters were obtained from the LigParGen web server, while the atomic charges for the Li^+ cation and PF_6^- anion were scaled by a factor of 0.7 to account for polarization effects.[23,24] The van der Waals interactions were described using a Lennard-Jones potential with a cutoff of 10 Å, and electrostatics were treated using the particle-particle particle-mesh (P3M) solver, with a 10 Å real-space cutoff and a relative error of 0.01% in the computed forces.

Prior to the production run, we implemented a multi-stage equilibration protocol to ensure proper relaxation. First, energy minimization was performed using the conjugate gradient algorithm, to eliminate any unphysical geometries. This was followed by an NPT compression step, at 10 K and 100 atm for 5 ps. The system was then gradually heated to 400 K and decompressed to 1 atm over another 5 ps, followed by an additional 5 ps NPT equilibration at these conditions. Subsequently, the system was cooled to 298 K over 5 ps and equilibrated in the NPT ensemble for 2 ns. A further 2 ns equilibration in the NVT ensemble at the target was performed temperature before proceeding to the production phase. The production trajectory was run for 200 ns in the NVT ensemble. Throughout all stages, thermostat and barostat damping parameters were set to 1 ps, and the integration timestep was 1 fs.

During the production phase, atomic coordinates were recorded every 0.2 ns. Trajectory analysis was performed using MDAnalysis package in Python.[25] To characterize the spatial orientation of COF atoms around sodium ions, we defined a polar angle as follows. The sodium ion is set at the origin of a new reference frame with the XY plane aligned with that of the simulation box. The angle between the Z axis of this frame and the vector connecting the sodium ion to a nearby COF atom is defined as the polar angle. Only COF atoms within the first coordination shell of the sodium ions were considered in the angle distribution analysis. The coordination shell was defined using the sodium radial distribution function (RDF), with a cutoff radius of 5.14 Å. This cutoff radius was used to calculate the reported coordination numbers (CNs).

Equation S1

$$D = \frac{2\pi}{q} \quad \text{(S1)}$$

Table S 1: Electrochemical performance comparison of DAAQ-TFP COF with COFs based cathodes for SIBs.

COF	Specific Capacity (mAh g^{-1})	Capacity retention	Reference
TQBQ-COF	452 at 0.02 A g^{-1}	96% after 1000 cycles at 1.0 A g^{-1}	[9]
Aza-COF	545 at 0.06 A g^{-1}	87% after 500 cycles at 5C	[10]
S@TAPT-COF	109.3 at 0.1 A g^{-1}	63% after 2000 cycles at 2.0 A g^{-1}	[11]
COF@CNT-50	164 at 0.025 A g^{-1}	69% after 1000 cycles at 0.5 A g^{-1}	[12]
BPOE	230 at 0.01 A g^{-1}	80% after 40 cycles at 0.1 A g^{-1}	[13]
TPAD-COF	64.7 at 0.2 A g^{-1}	98% after 450 cycles	[26]
DAAQ-TFP COF	120 at 0.3 A g^{-1}	91.2 % after 4775 cycles at 0.3 A g^{-1}	This work

Table S 2: Electrochemical performance comparison of DAAQ-TFP COF with DAAQ based cathodes for SIBs.

Name	Specific Capacity (mAh g^{-1})	Capacity retention	Reference
P11	165 at 0.05 A g^{-1}	92% after 150 cycles at 0.05 A g^{-1}	[14]
P12	192 at 0.05 A g^{-1}	95% after 500 cycles at 0.05 A g^{-1}	[14]
AQ26ONa	142 at 0.05 A g^{-1}	70% after 50 cycles at 0.05 A g^{-1}	[15]
Na_2AQ26DS	120 at 0.05 Ag^{-1}	72% after 1000 cycles at 1 A g^{-1}	[16]
AQS	209 at 0.03 A g^{-1}	44% after 100 cycles at 0.03 A g^{-1}	[17]
AQDS	195 at 0.03 A g^{-1}	67% after 100 cycles at 0.03 A g^{-1}	[17]
DAAQ-TFP COF	120 at 0.3 A g^{-1}	91.2 % after 4775 cycles at 0.3 A g^{-1}	This work

Table S 3: COF unit cell parameters and Pawley refinement results, along with key details of the experimental setup used for data collection.

Pawley refinement	
Software	HighscorePlus
Cu Kα radiation wavelength (Å)	1.54060
Pattern range, 2θ (°)	3.0001 – 35.9801
Crystal system	Hexagonal
a=b, c (Å)	28.66 (5), 3.628 (5)
α=β, γ (°)	90, 120
T (°C)	25
Weighted profile R-factor, Rwp (%)	2.63
Goodness of Fit, GOF	1.56

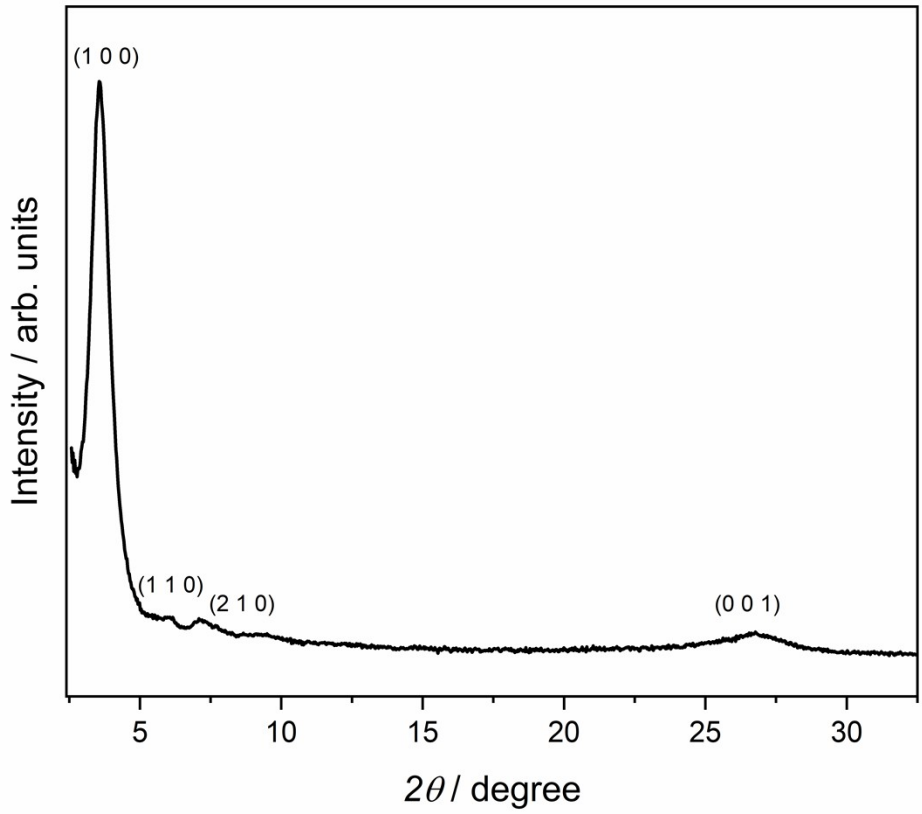

Figure S 1: WAXS analysis performed on DAAQ-TFP powder, revealing diffraction peaks at 3.5°, 5.9°, 7.0°, and 26.0°, corresponding to the (100), (110), (210), and (001) crystal planes, respectively.

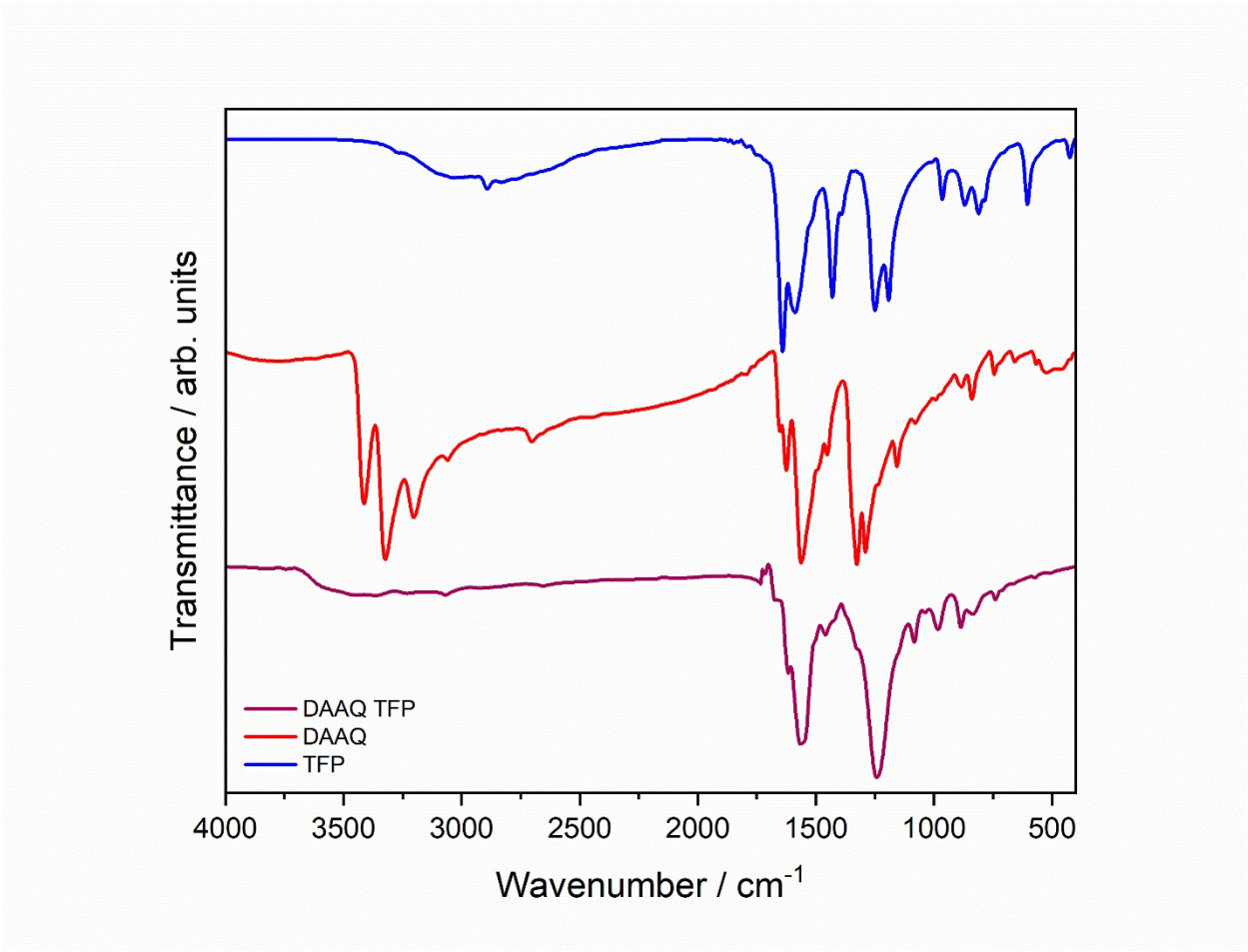

Figure S 2: FT-IR spectra of TFP (blue), DAAQ (red) and DAAQ-TFP (purple).

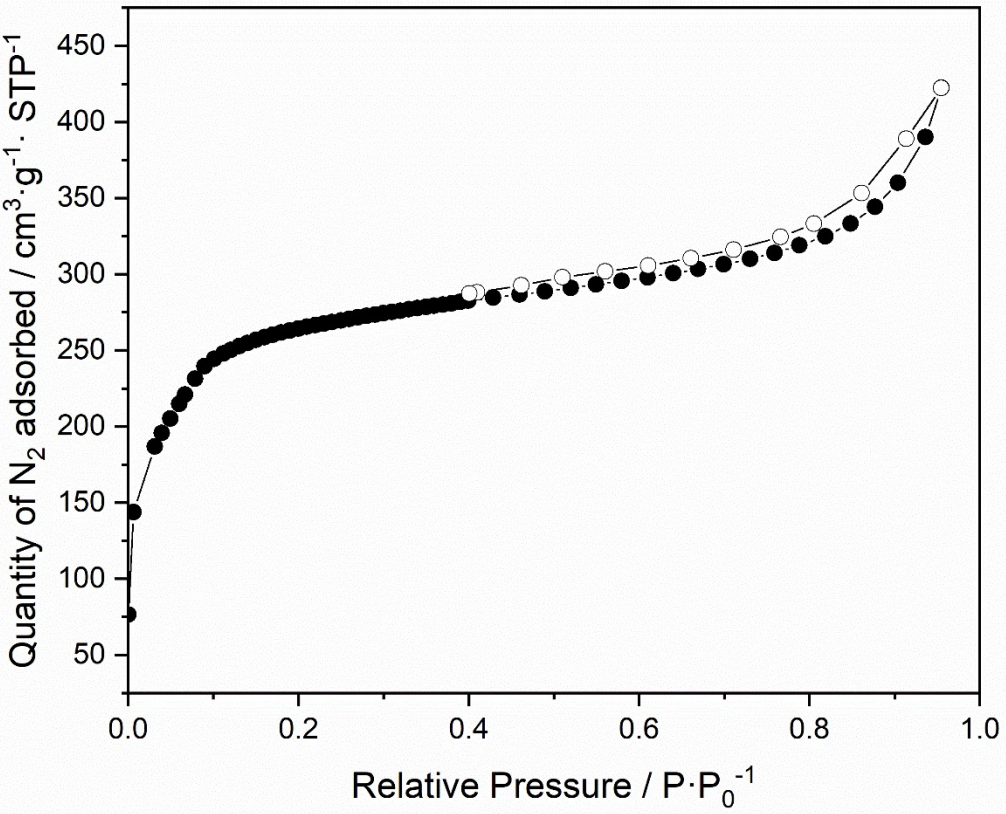

Figure S 3: Nitrogen adsorption-desorption isotherm of DAAQ-TFP.

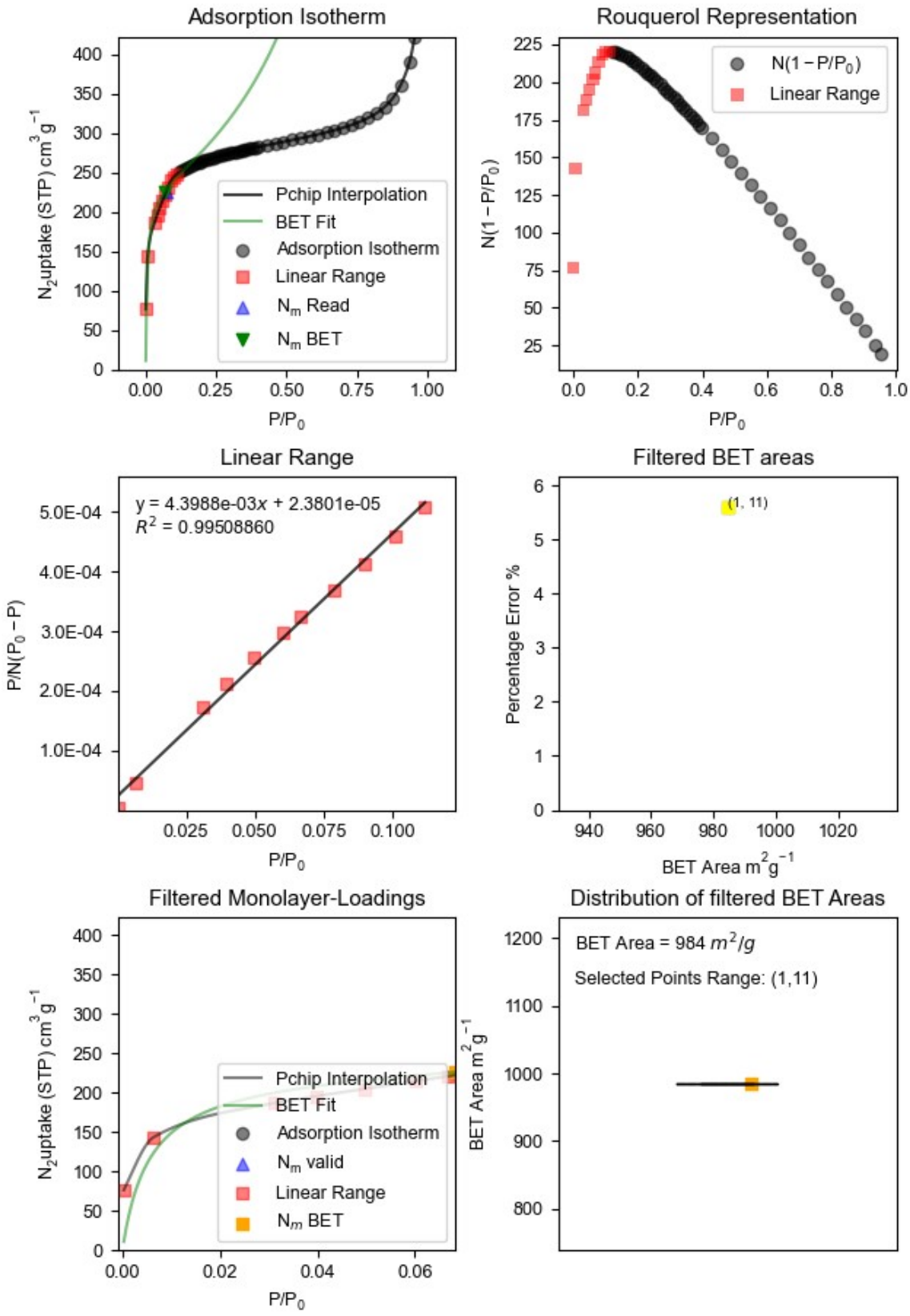

Figure S 4: BETSI analysis for DAAQ-TFP COF.

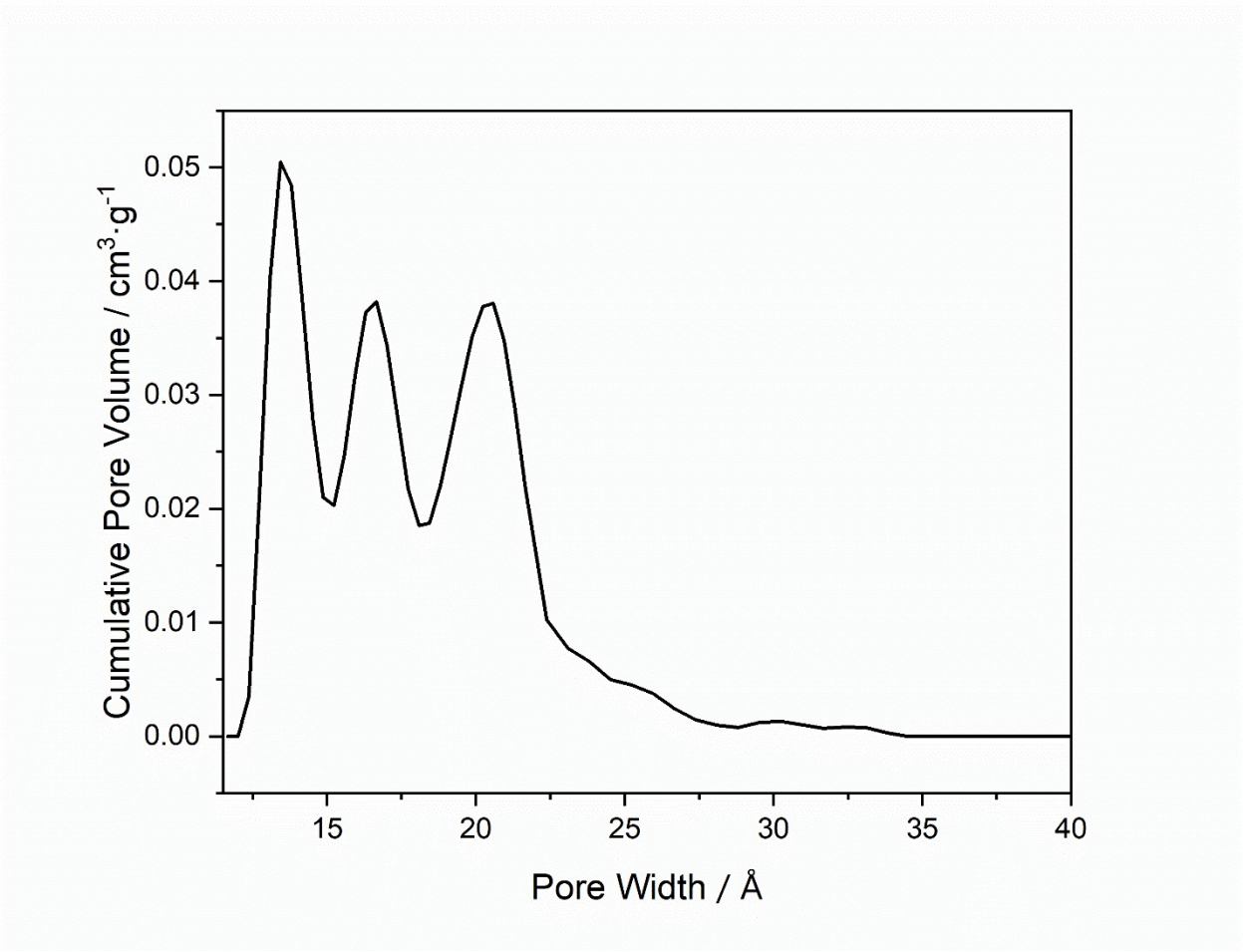

Figure S 5: Pore size distributions of DAAQ-TFP characterized by nitrogen adsorption-desorption isotherm.

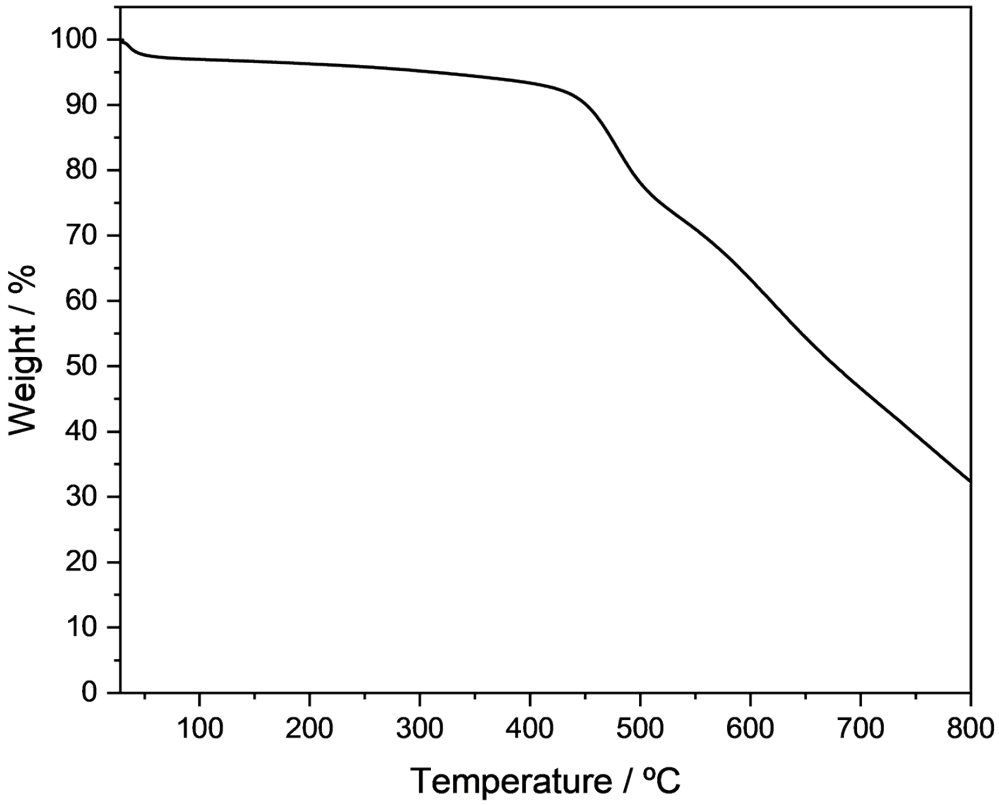

Figure S 6: TGA profile of DAAQ-TFP COF.

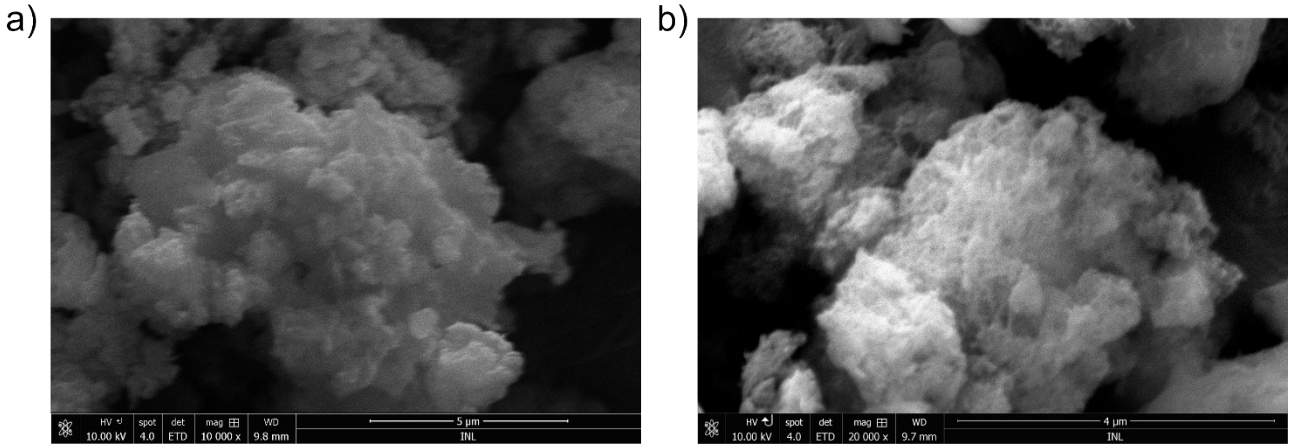

Figure S 7: SEM images of DAAQ-TFP powder at (a) mag 10 000 x and (b) mag 20 000 x.

Table S 4: DAAQ-TFP powder EDX analysis.

Element	Weight (%)	Atomic (%)
C	61.4	72.4
N	10.0	10.2
O	17.4	16.6
Au*	11.2	0.8

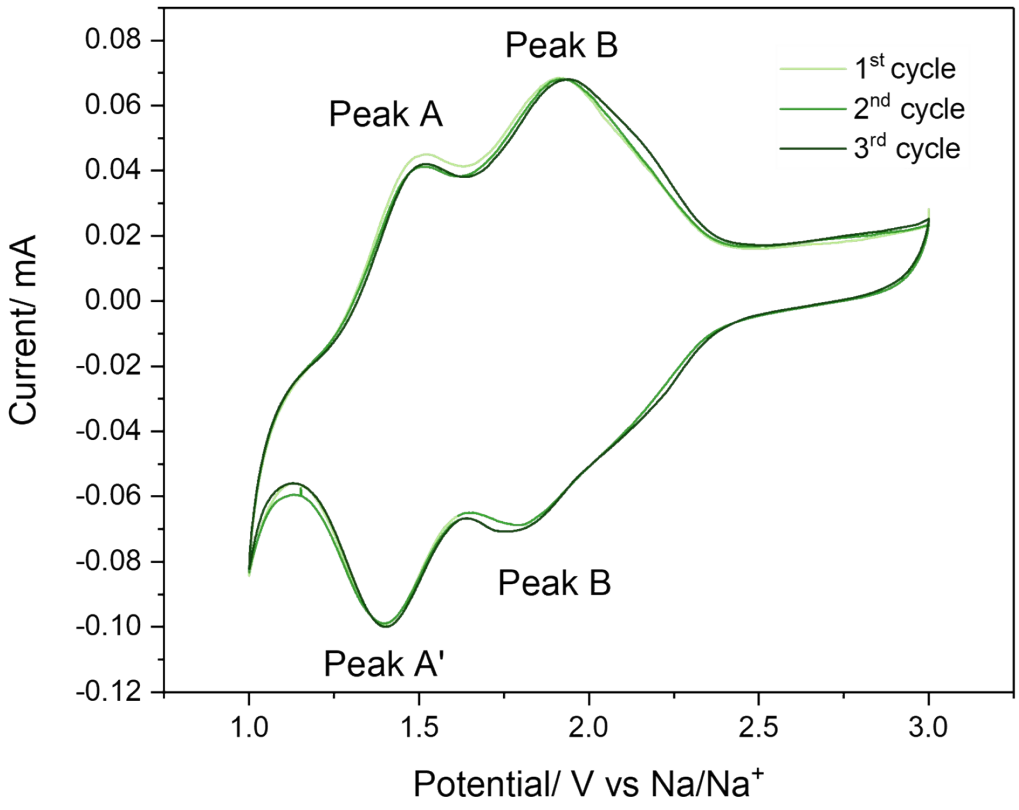

Figure S 8: CV profiles with indexed peaks recorded at the 1st, 2nd and 3rd cycle in the 1-3 voltage window.

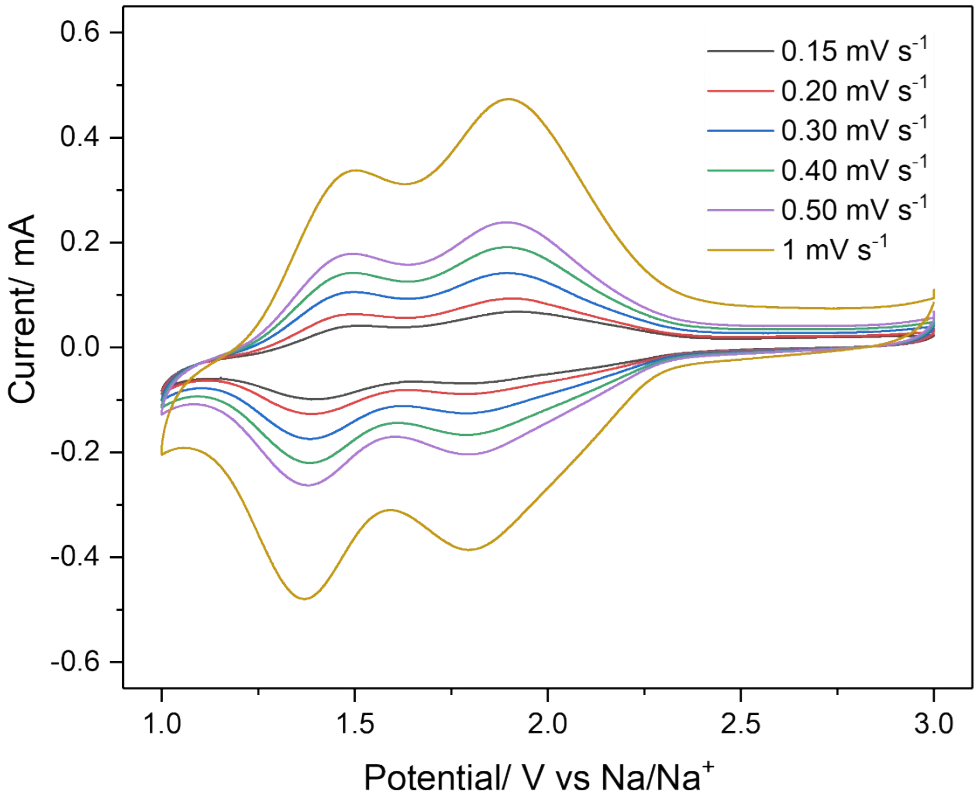

Figure S 9: Cyclic voltammetry profiles at different scan rates (0.15, 0.20, 0.30, 0.40, 0.50 and 1 mV s^{-1}) recorded in the 1-3 potential window.

Equation S2

$$I = av^b \quad \text{(S2)}$$

Equation S3

$$Log(I) = bLog(v) + Log(a) \quad \text{(S3)}$$

Where:

a and *b* are the intercept and the slope of the linear fit, respectively.

Equation S4

$$I_p = 0.4463zFAC\sqrt{\frac{zF\nu D_{CV}}{RT}} = 2.686 \cdot 10^5 AC\sqrt{z^3\nu D_{CV}} \quad \text{(S4)}$$

Where:

I_p is the peak current value, z is the number of exchanged electrons, F is the Faraday constant, A is the electrode area, C is the Na^+ concentration, v is the scan rate, R is the gas constant, and T is the temperature.

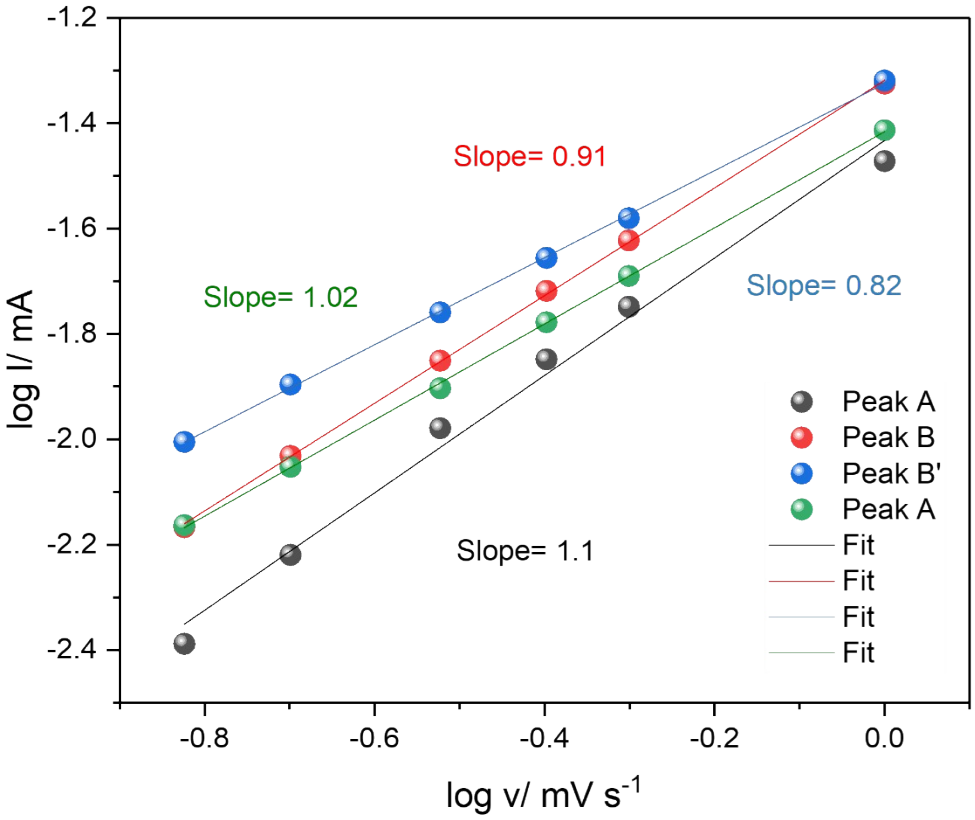

Figure S 10: logarithm of intensity vs logarithm of the scan rate with slope value obtained by the linear fit.

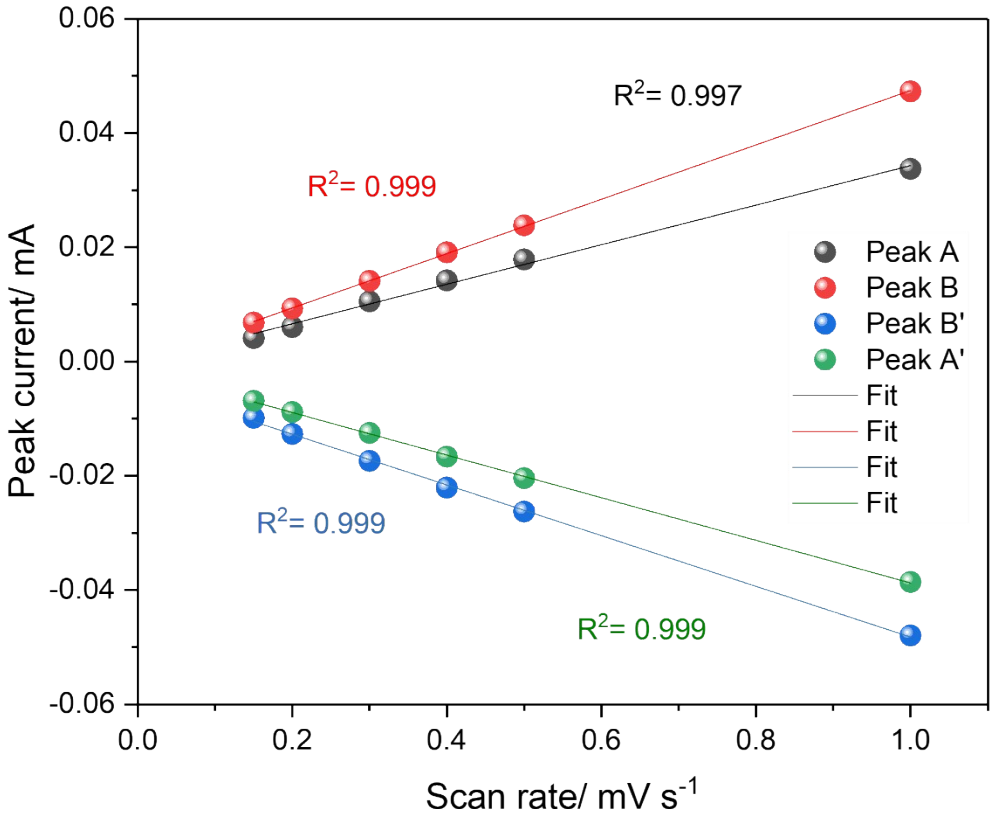

Figure S 11: Peak current vs. scan rate and related linear fit.

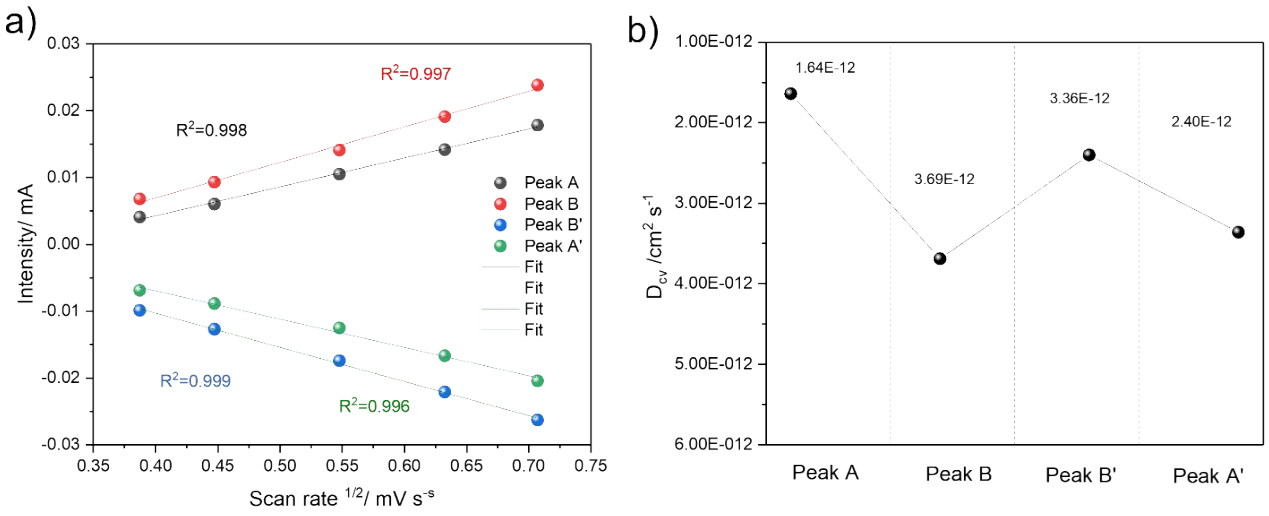

Figure S 12: (a) Peak current vs. square root of scan rate and related linear fit. (b) Trend of the diffusion coefficient.

Equation S5

$$I(V) = k_1 v + k_2 v^{1/2} \quad \text{(S5)}$$

Equation S6

$$I(V)\, v^{-1/2} = k_1 v^{1/2} + k_2 \quad \text{(S6)}$$

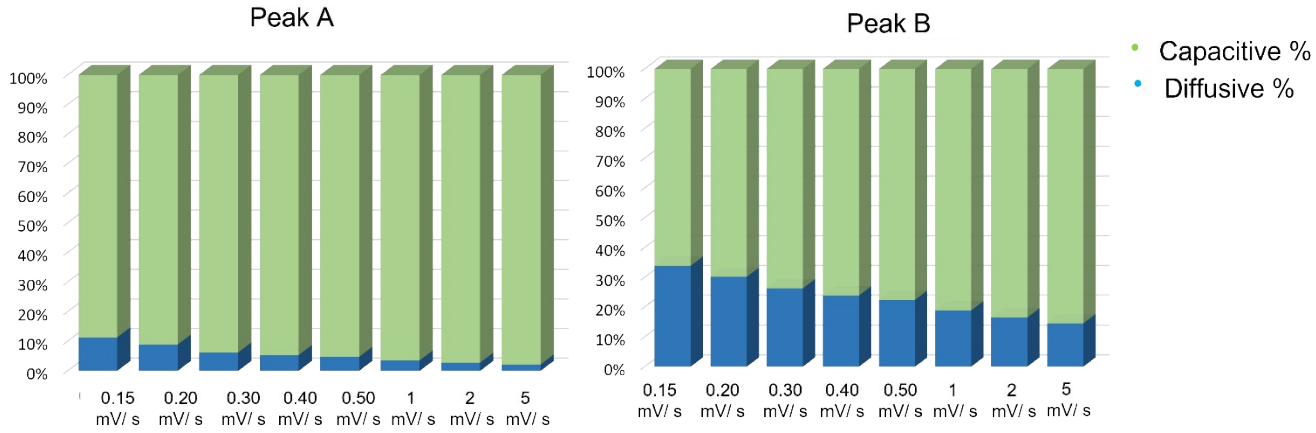

Figure S 13: Capacitive and diffusive contribution calculated from CV at different scan rate for (a) peak A and (B) Peak B.

For each impedance measurement, the total harmonic distortion (THD) (**Figure S14a**) and non-stationary distortion (NSD) (**Figure S14b**) were monitored. The THD I% and NSD I% data for the AC response show values below 5% at all states of charge (SoCs) and frequencies, thus confirming that the measurements were performed under reliable conditions, with a linear response and always in equilibrium.[27,28]

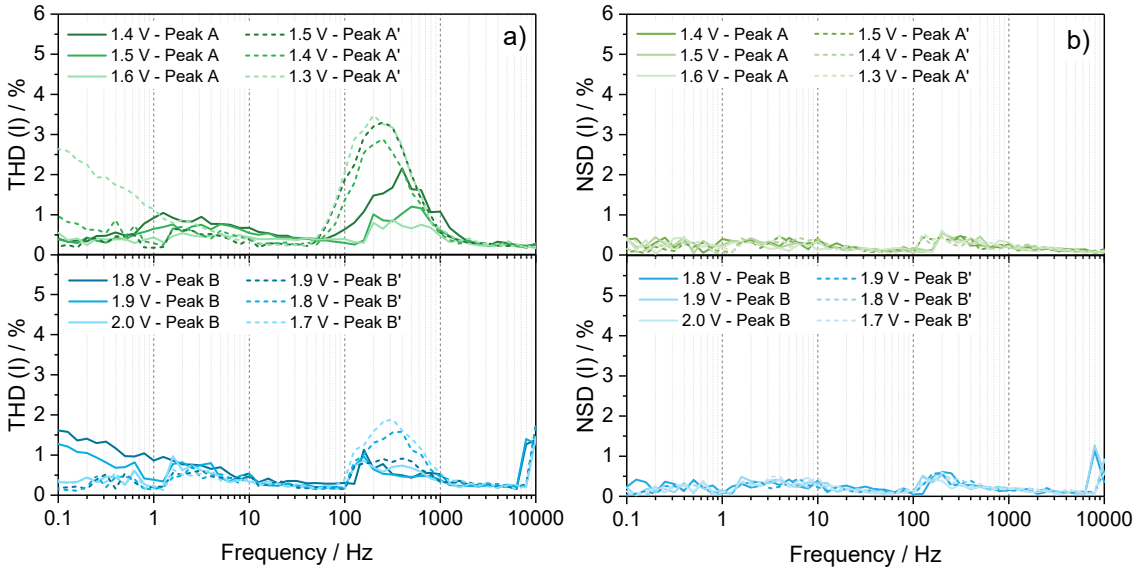

Figure S 14: total harmonic distortion (a) and non-stationary distortion (b) trend to ensure that both linearity and stationarity boundary conditions are met.

Boundary conditions require the convergence of the angular frequency towards the real axis ($\omega \rightarrow 0$). Therefore, prior to the calculation, the dispersions were fitted to the equivalent circuit $R_{el}(R_{ct}Q_{dl})WQ$, according to Boukamp's notation, where R_{el} represents the resistance of the electrolyte, $(R_{ct}Q_{dl})$ represents the charge transfer resistance in parallel to the double-layer non-ideal capacitance and WQ represents the solid-state diffusion with charge accumulation.[29,30] After fitting, the low-frequency WQ element was subtracted from the raw spectra. [31,32]

To balance an optimal deconvolution with the suppression of artifact peaks, an optimized value of the regularization parameter λ = 0.01 was employed for both the DRT and DDC calculations (**Figure S15 a,b**) as described in the Supporting Information. [33] For the DDC plots associated with peaks A and A' (**Figure 2f,h**) and the DRT plots associated with peaks B and B' (**Figure 2g,i**), both distribution functions H(τ) and G(τ), respectively, expressed as a function of the relaxation frequency ($f = 1/2\pi\tau$), display the presence of one Gaussian only indicating the presence of one single process. For the sake of clarity, the mathematical transformation of **Equation 2** includes a *1/ω* factor, which "stretches" the frequency scale when moving from impedance to capacitance domain.[34] Hence, the presence of the DDC Gaussian at lower frequencies as compared to the DRT is mostly a result of mathematical data processing by the software rather than a slower kinetics of the associated process. Nevertheless, the obtained results indicate that, for each signal observed during galvanostatic cycling (peaks A/A' and B/B'), only one capacitive process and one faradaic process occurs.

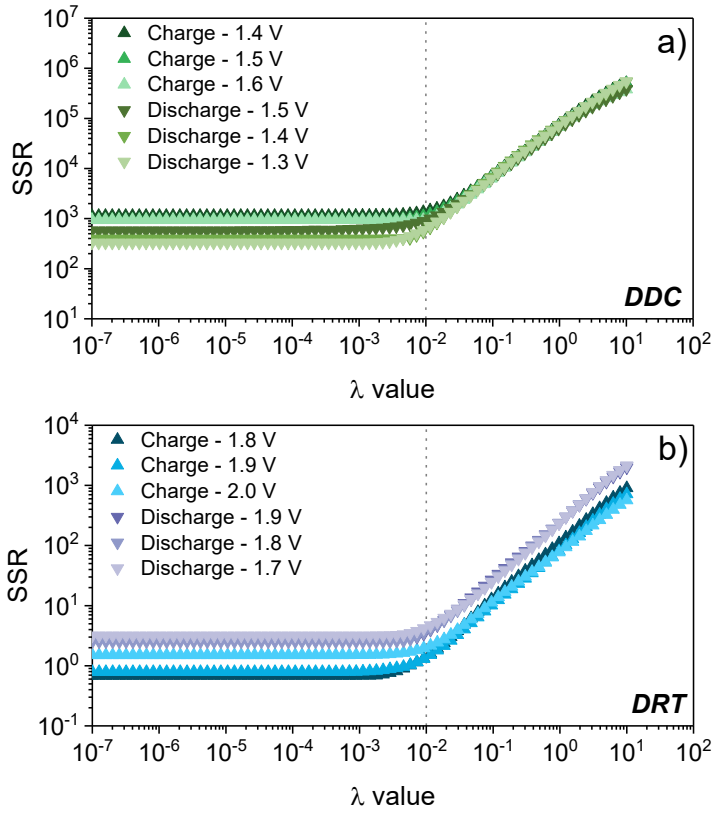

Figure S 15: Sum of squared residuals (SRR) vs lambda plot for optimized calculation of (a) DDC function and (b) DRT functions.

Equation S7

$$n\lambda = 2dsin\theta \quad \text{(S7)}$$

Table S 5: d- spacing values calculated from 001 diffraction plane for the powder, the pristine, sodiated and desodiated electrodes.

Sample	d-spacing (Å) from 001 plane
Pristine	3.40
Sodiated	3.47
Desodiated	3.46

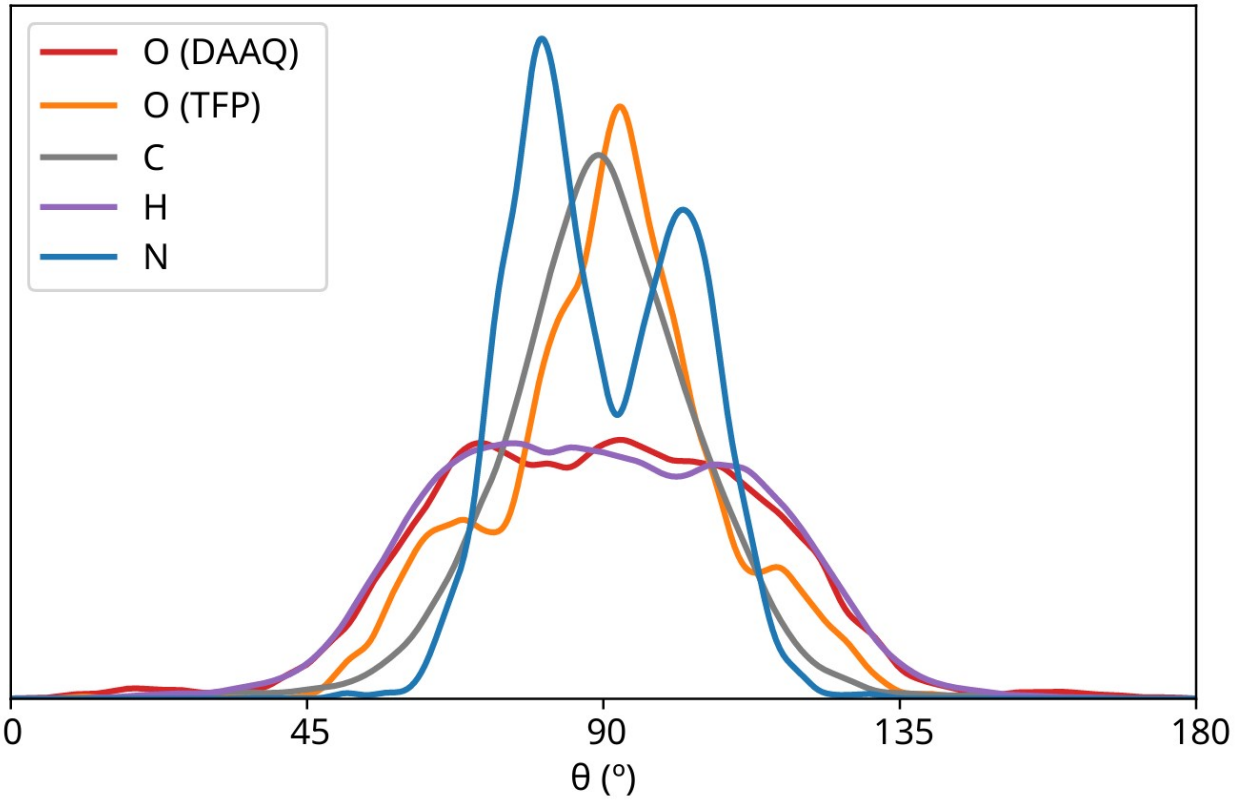

Figure S 16: Distribution of the polar angle defined by the sodium ions and different COF elements within the first sodium coordination shell, as described in the SI.

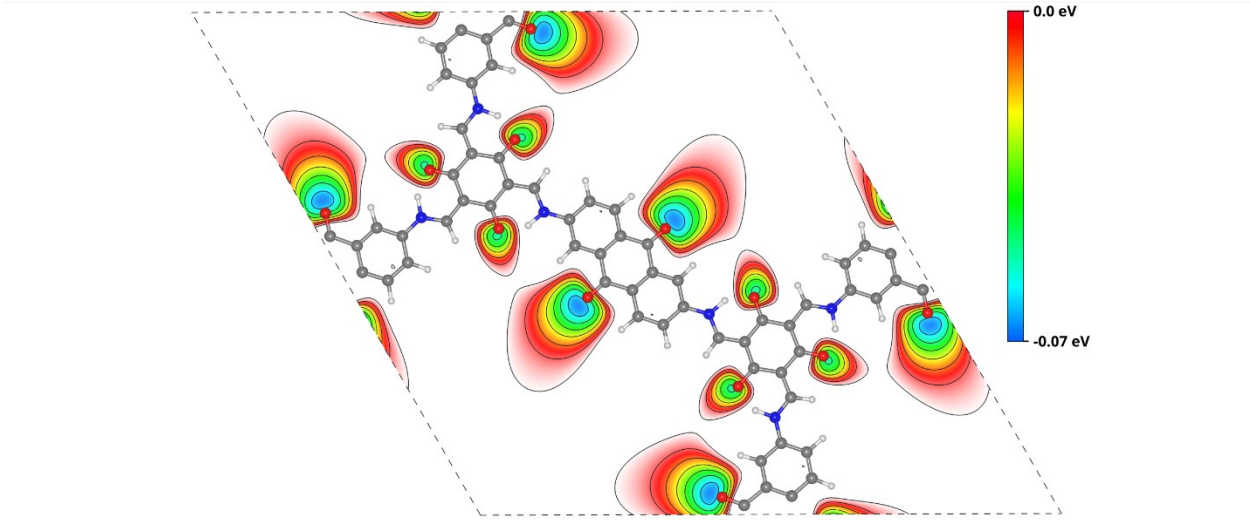

Figure S 17: Electrostatic potential (defined as the sum of the Hartree potential and the local pseudopotential) of the DAAQ-TFP-COF structure in the interlayer plane. Only the negative values of the potential are colored.

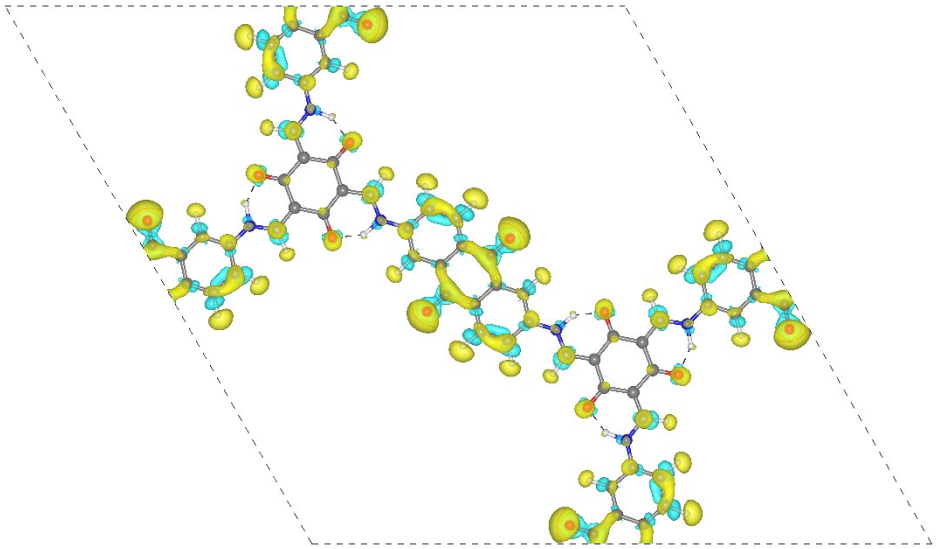

Figure S 18: Difference in the electron density between the reduced and the neutral DAAQ-TFP-COF structure (isosurface value 5x10⁻⁴ Å³). Positive values are shown in yellow, negative values in blue.

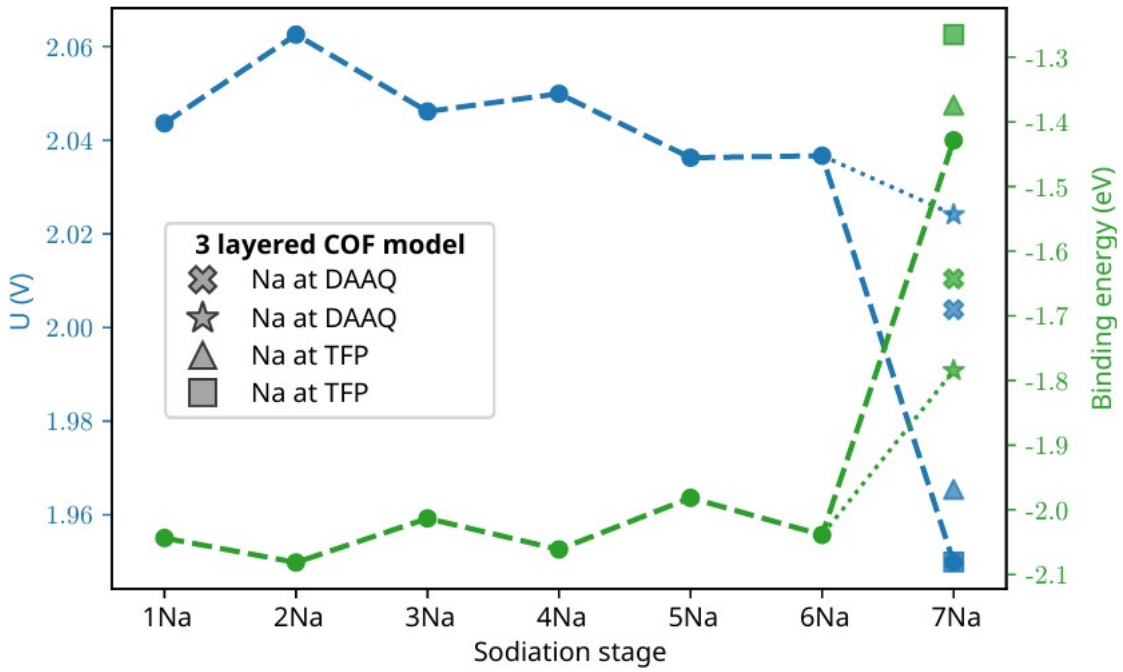

Figure S 19: Reduction potential and binding energy of the DAAQ-TFP-COF at subsequent sodiation stages. Circles correspond to the most energetically favorable configurations in a two-layer COF system at each stage. Different symbols at the seventh stage are calculated with a three-layer COF system, each symbol corresponding to a different position for the seventh sodium atom.

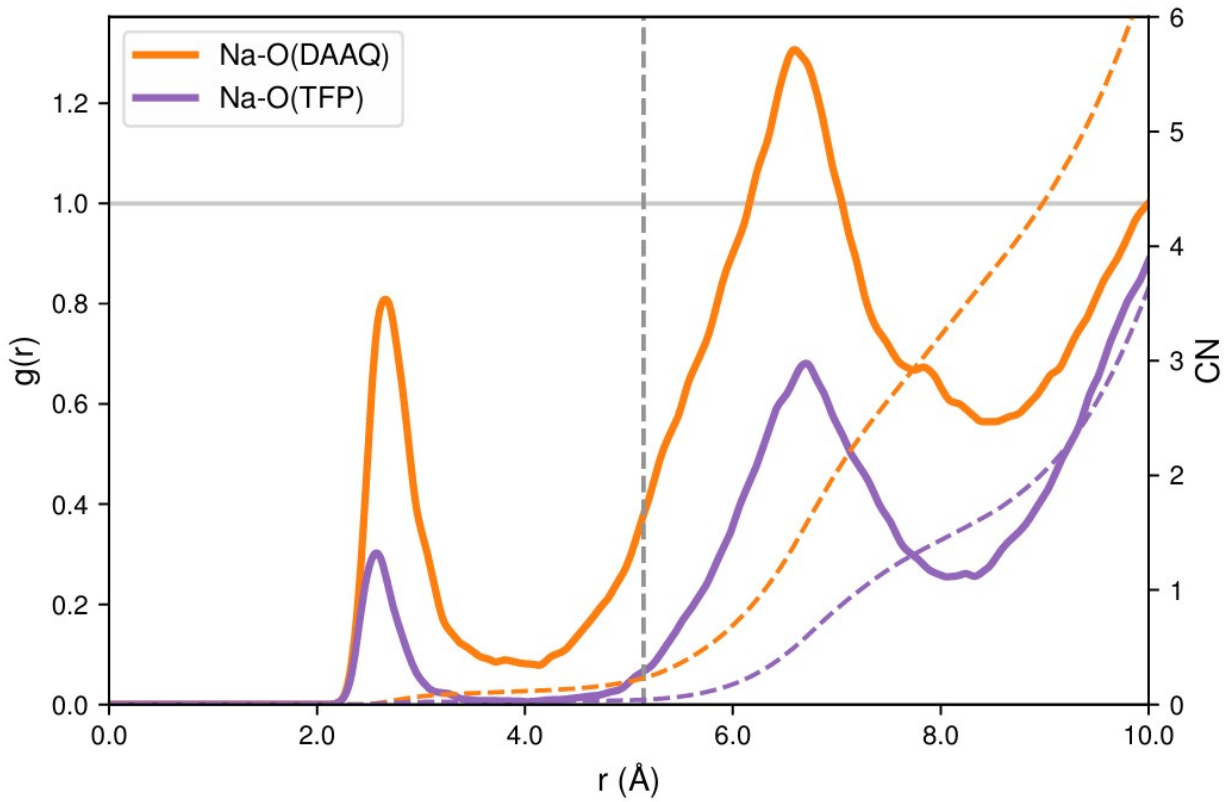

Figure S 20: RDFs (solid lines) and CNs (dashed lines) between sodium ions and DAAQ and TFP oxygen atoms. The vertical dashed line indicates the cutoff for the first coordination shell.

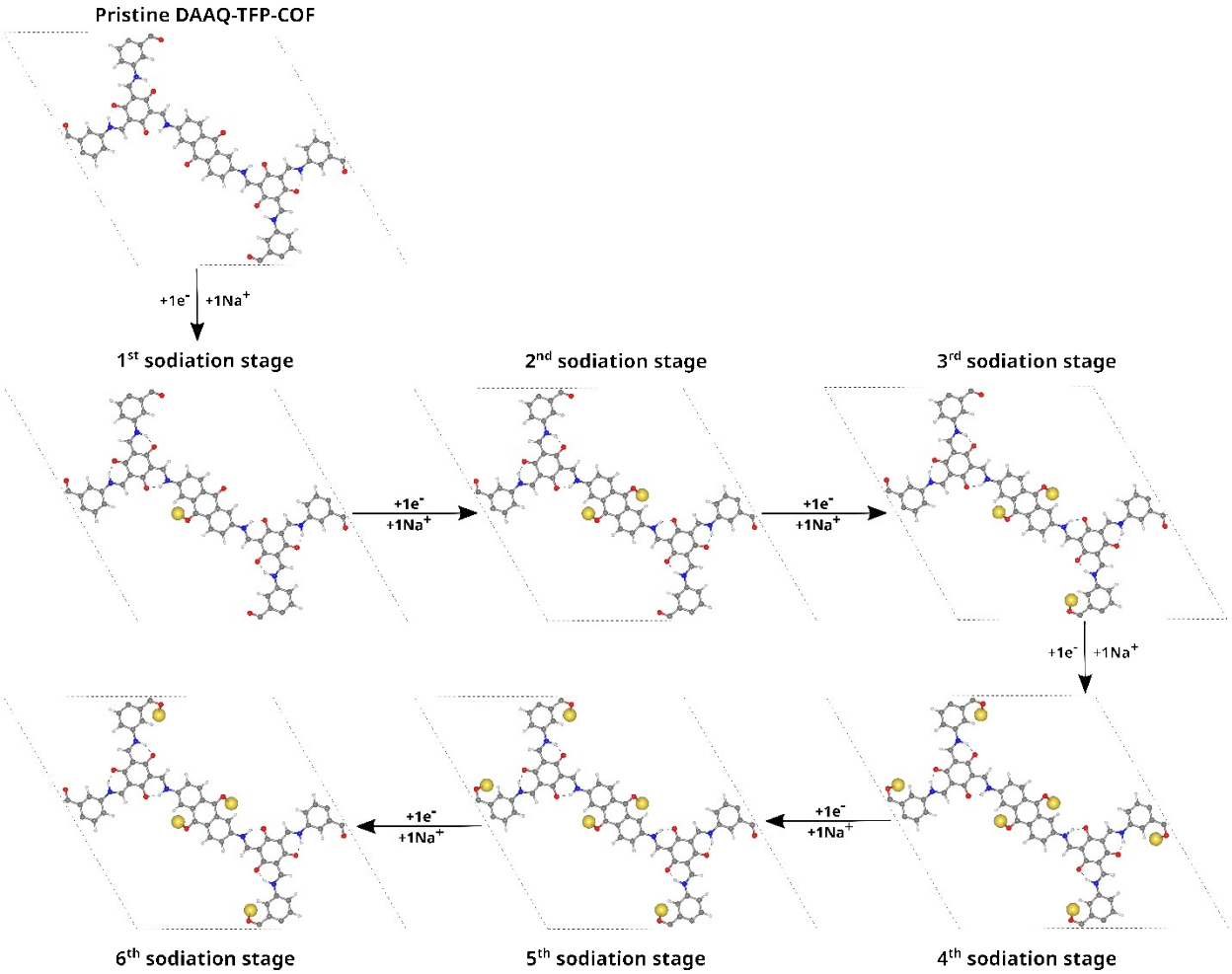

Figure S 21: Sodiation steps of the DAAQ-TFP COF.

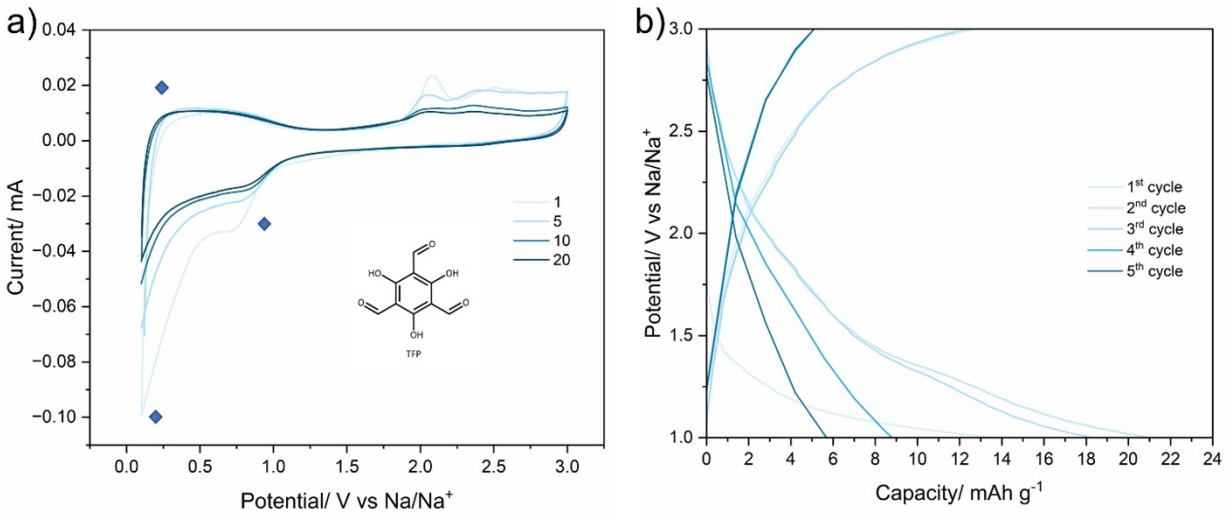

Figure S 22: Electrochemical performance of the TFP molecule. (a) Cyclic voltammetry curves recorded at various cycles (1st, 5th, 10th, and 20th), with peaks not attributable to the organic molecule indicated with blue squares. (b) Galvanostatic charge-discharge profiles over the first five cycles.

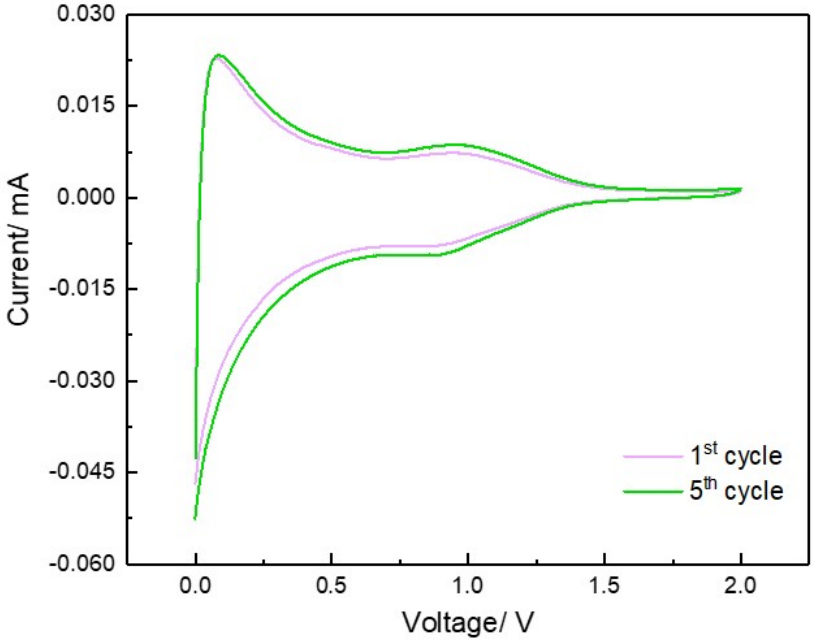

Figure S 23: Cyclic voltammetry curves of 90% carbon black electrodes.

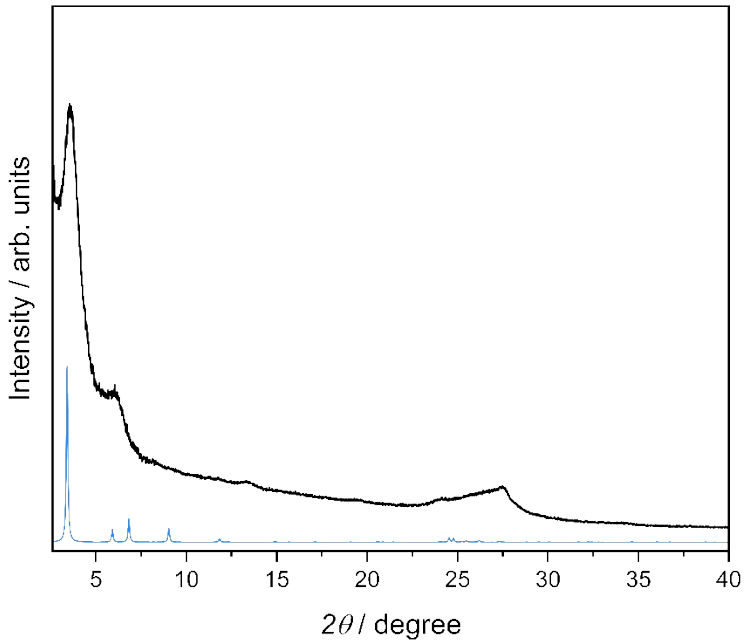

Figure S 24: XRD pattern of Da TFP COF (black) and corresponding AA-stacking model simulation (blue).

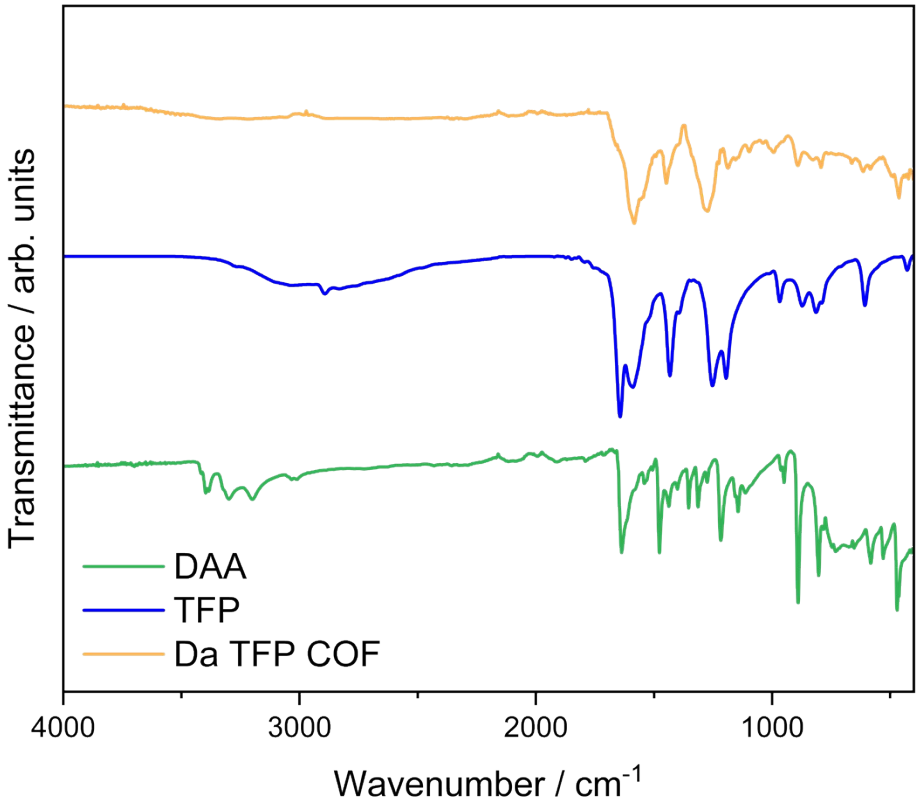

Figure S 25: FT-IR spectra of TFP (blue), DAA (green) and Da TFP (orange) confirm the successful synthesis.

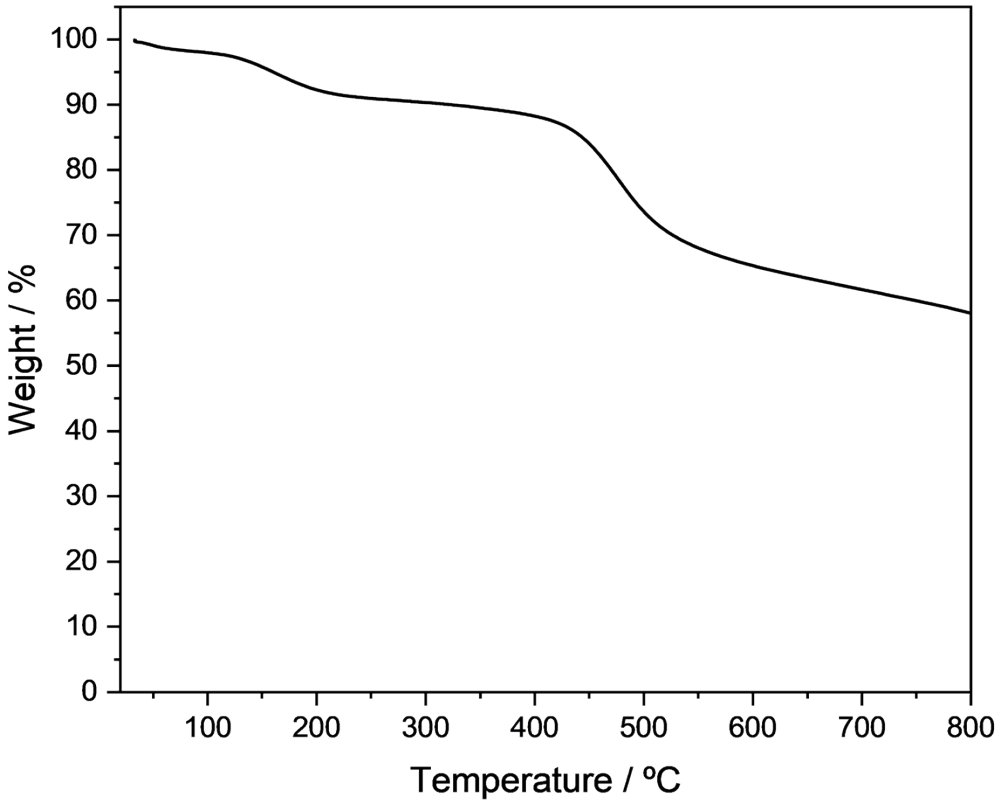

Figure S 26: TGA of Da TFP-COF.

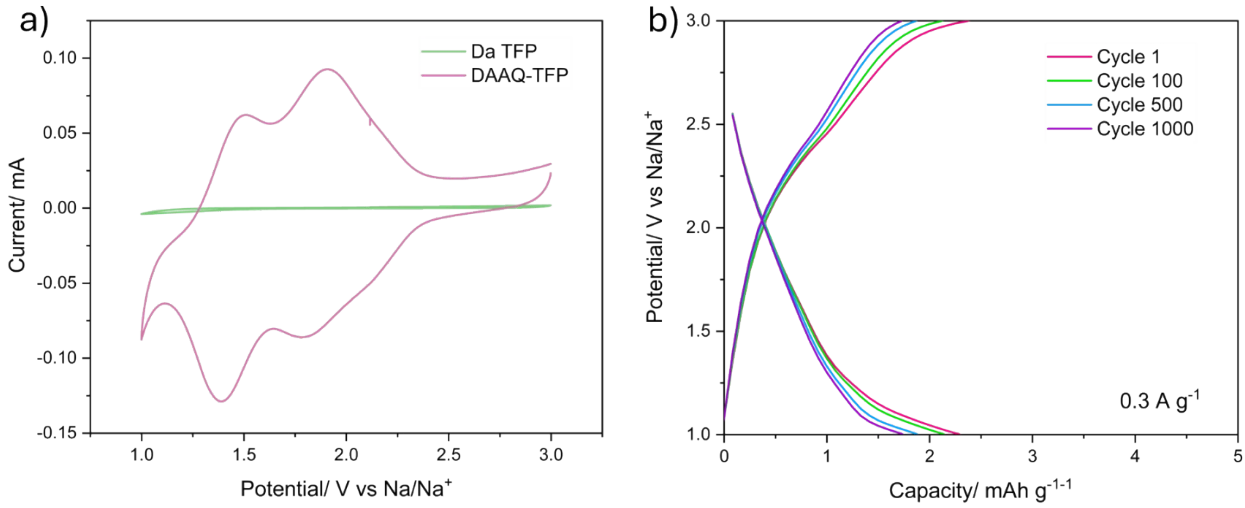

Figure S 27 : (a) Comparison between the cyclic voltammetry curves of DAAQ-TFP and Da TFP COFs at a scan rate of 0.2 mV s $^{-1}$. (b) Selected galvanostatic charge–discharge profiles of Da TFP COF.

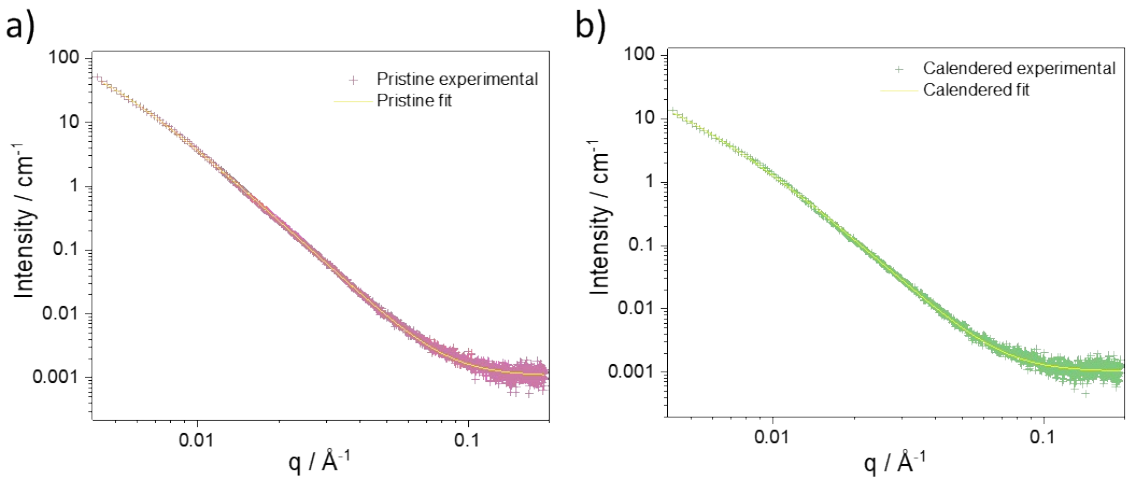

Figure S 28: SAXS fitting profiles highlighting morphological features of the electrodes. (a) Low-q region for the pristine electrode. (b) Low-q region for the calendered electrode.

Table S 6: Summary of SAXS fitting parameters for pristine and calendered electrodes.

	Pristine electrode	**Calendered electrode**
Software	SasView 6.0.0	SasView 6.0.0
Model name	Mass_surface_fractal	Mass_surface_fractal
Q Range ($Å^{-1}$)	min = 0.00426599153 max = 0.191590419	min = 0.00426599153 max = 0.191590419
χ^2	4.5	3.6
Fractal_dim_mass	0.0697 ± (2)	1.56 (5)
Fractal_dim_surf	2.090 (8)	2.180 (8)
Rg_cluster	1157 (8)	1350 (8)
Rg_primary	692.5 (1)	277 (9)

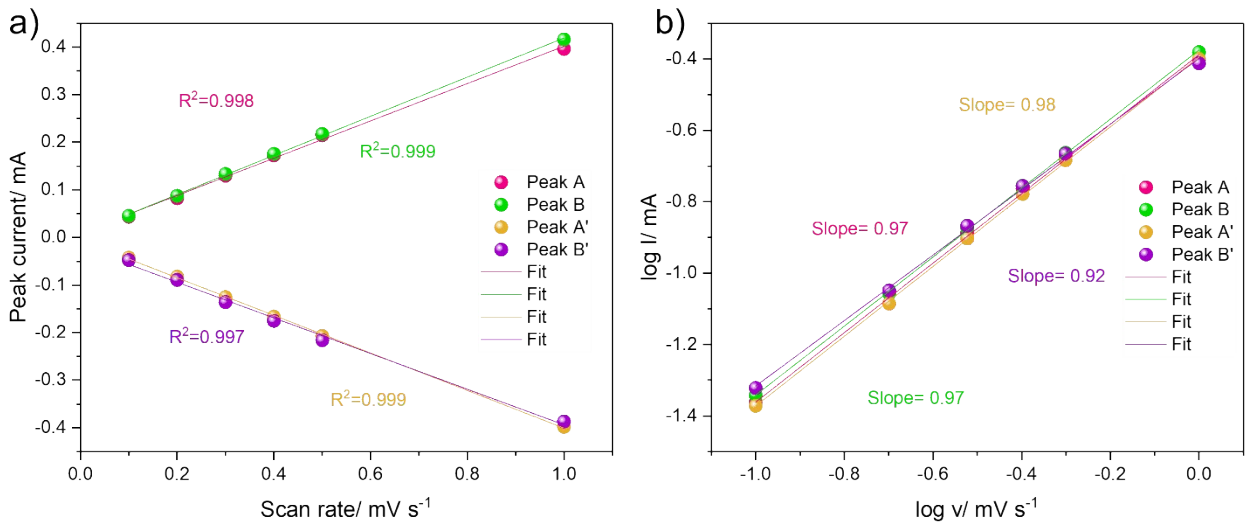

Figure S 29: (a) Peak current vs. scan rate with related linear fit and (b) logarithm of intensity vs logarithm of the scan rate with slope value obtained by the linear fit obtained from the CVs of the calendared electrode (volume reduction 50%).

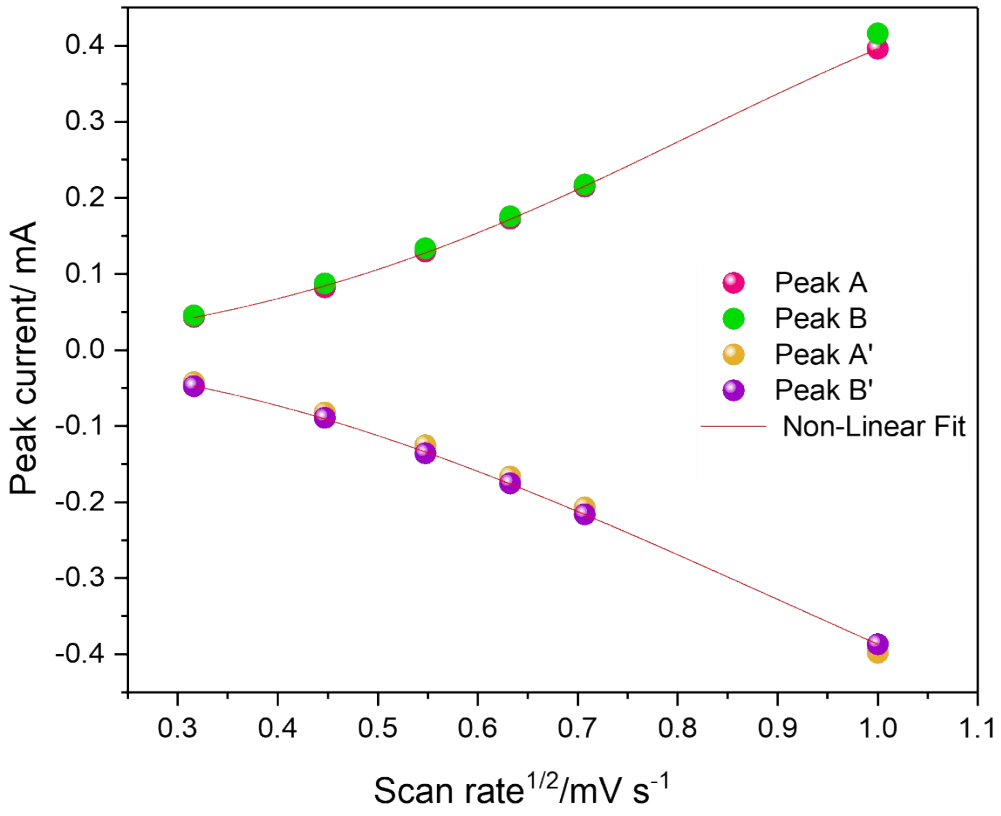

Figure S 30: Peak current vs. square root of scan rate and related non-linear fit for the calendared electrode (volume reduction 50%).

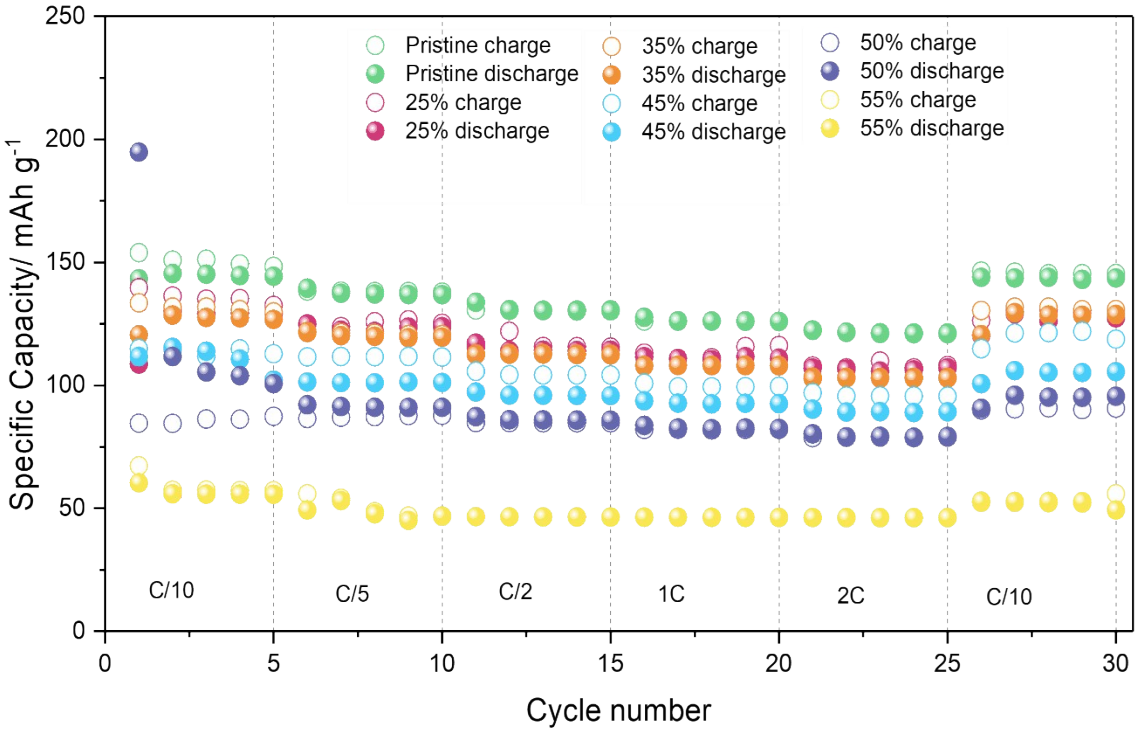

Figure S 31: Rate capability tests at different scan rates performed on the pristine (green), and calendared electrodes with a volume reduction of 25% (red), 35% (orange), 45% (light blue), 50% (blue) and 55% (yellow).

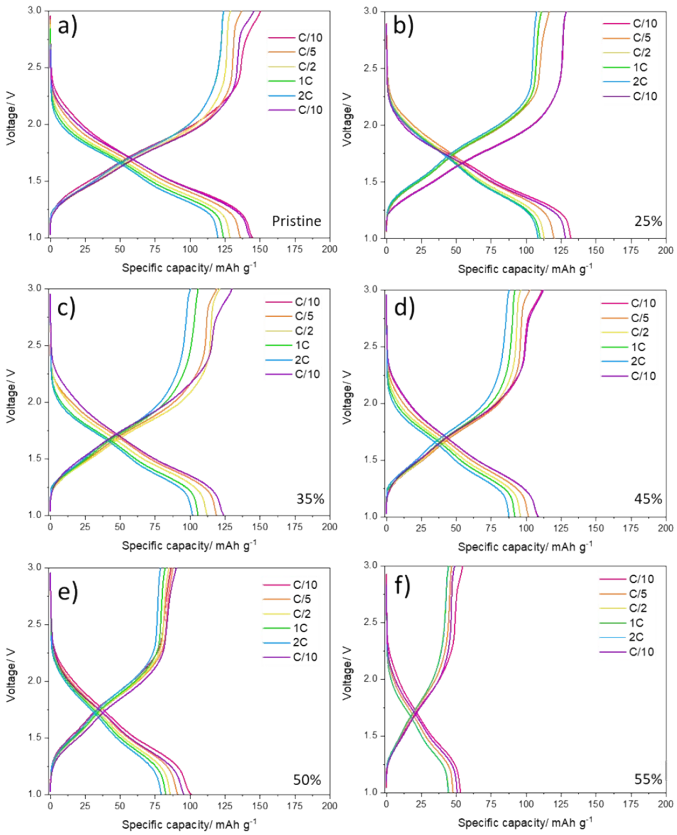

Figure S 32: Galvanostatic charge–discharge profiles of the pristine electrode and electrodes with varying volume-reduction percentages resulting from calendering.

Table S 7: Cathode utilization as a function of C-rate.

C-rate	**Capacity (mAh·g⁻¹)**	**Utilization** (%)
C/10	145	96%
C/5	136	90%
C/2	130	86%
1C	125	83%
2C	121	80%
C/10	143	95%

Table S 8: Cathode utilization as a function of calendaring.

Volume reduction	**Capacity (mAh·g⁻¹)**	**Utilization (%)**
Pristine	145	96%
25%	130	86%
35%	126	84%
45%	102	68%
50%	100	66%
55%	55	36%

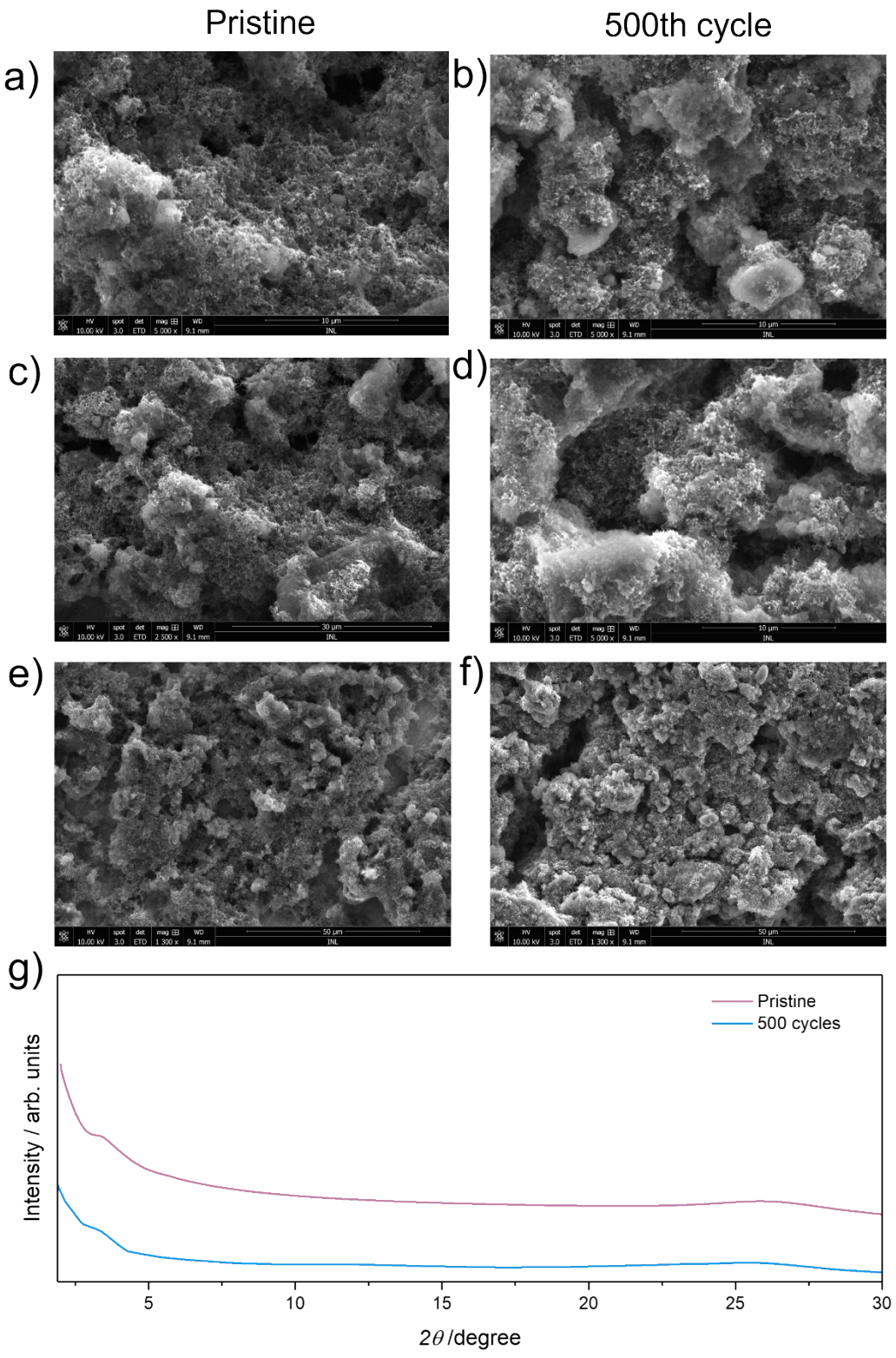

Figure S 33: SEM images at different magnifications (a,c,e) for the pristine electrode and (b,d,f) for the electrode after 500 charge-discharge cycles. (g) XRPD patterns of pristine electrode (purple) and of ex-situ electrode after 500 cycles (light blue).

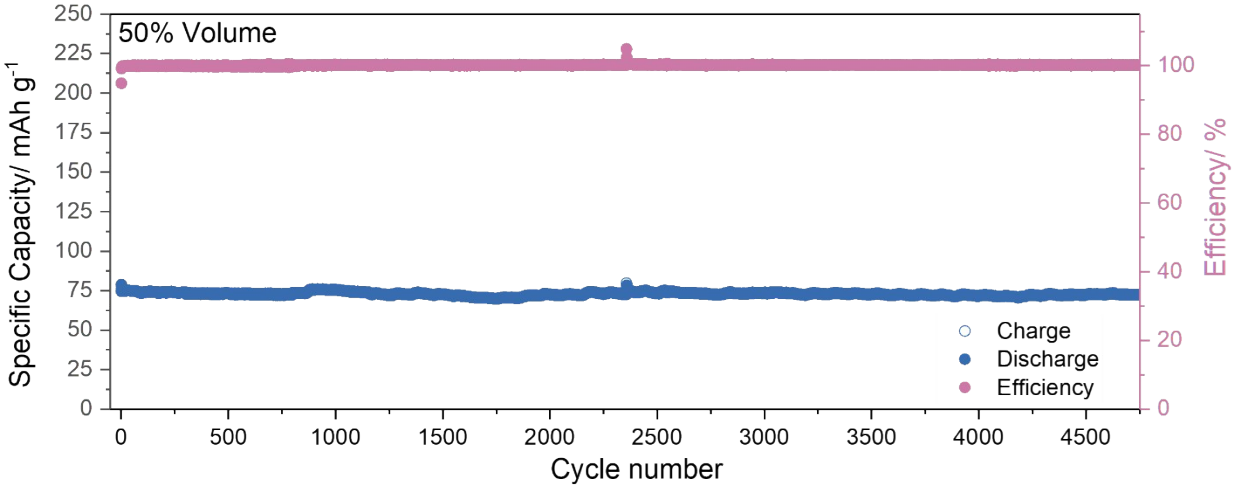

Figure S 34: Long cycling performances and relative CE of the calendared electrode (volume reduction 50%) for 4750 charge-discharge cycles at 2C.

Bibliography

[1] S. Wang, Q. Wang, P. Shao, Y. Han, X. Gao, L. Ma, S. Yuan, X. Ma, J. Zhou, X. Feng, B. Wang, *J Am Chem Soc* 2017, *139*, DOI 10.1021/jacs.7b02648.

[2] J. Duan, W. Wang, D. Zou, J. Liu, N. Li, J. Weng, L. P. Xu, Y. Guan, Y. Zhang, P. Zhou, *ACS Appl Mater Interfaces* 2022, *14*, DOI 10.1021/acsami.2c04831.

[3] N.d.

[4] R. Shi, L. Liu, Y. Lu, C. Wang, Y. Li, L. Li, Z. Yan, J. Chen, *Nat Commun* 2020, *11*, DOI 10.1038/s41467-019-13739-5.

[5] U. De, S. De Compostela On, *J. Chem. Inf. Model* 2024, *64*, 33.

[6] P. W. Schmidt, *J Appl Crystallogr* 1991, *24*, DOI 10.1107/S0021889891003400.

[7] A. J. Hurd, D. W. Schaefer, J. E. Martin, *Phys Rev A (Coll Park)* 1987, *35*, DOI 10.1103/PhysRevA.35.2361.

[8] J. W. M. Osterrieth, J. Rampersad, D. Madden, N. Rampal, S. L. Griffin, B. Chen, R.-B. Lin, B. Coasne, S. Cohen, J. C. Moreton, Y. J. Colón, L. Chen, R. Clowes, F.-X. Coudert, Y. Cui, B. Hou, D. M. Alessandro, P. W. Doheny, M. Dincă, C. Sun, C. Doonan, M. T. Huxley, J. D. Evans, P. Falcaro, R. Ricco, O. Farha, K. B. Idrees, T. Islamoglu, P. Feng, H. Yang, R. S. Forgan, D. Bara, S. Furukawa, E. Sanchez, J. Gascon, S. Telalović, S. K. Ghosh, S. Mukherjee, M. R. Hill, M. Sadiq, P. Horcajada, P. Salcedo-Abraira, K. Kaneko, R. Kukobat, J. Kenvin, S. Keskin, S. Kitagawa, K.-I. Otake, R. P. Lively, S. J. A. Dewitt, P. Llewellyn, B. V Lotsch, S. T. Emmerling, A. M. Pütz, C. Martí-Gastaldo, N. M. Padial, J. García-Martínez, N. Linares, D. Maspoch, J. A. Suárez Del Pino, P. Moghadam, R. Oktavian, R. E. Morris, P. S. Wheatley, J. Navarro, C. Petit, D. Danaci, M. J. Rosseinsky, A. P. Katsoulidis, M. Schröder, X. Han, S. Yang, C. Serre, G. Mouchaham, D. S. Sholl, R. Thyagarajan, D. Siderius, R. Q. Snurr, R. B. Goncalves, S. Telfer, S. J. Lee, V. P. Ting, J. L. Rowlandson, T. Uemura, T. Iiyuka, M. A. Van Derveen, D. Rega, V. Van Speybroeck, S. M. J. Rogge, A. Lamaire, K. S. Walton, L. W. Bingel, S. Wuttke, J. Andreo, O. Yaghi, B. Zhang, C. T. Yavuz, T. S. Nguyen, F. Zamora, C. Montoro, H. Zhou, A. Kirchon, D. Fairen-Jimenez, J. W. M. Osterrieth, J. Rampersad, D. Madden, N. Rampal, B. Connolly, D. Fairen-Jimenez, *Adv. Mater* 2022, *2022*, 2201502.

[9] B. BOUKAMP, *Solid State Ion* 1986, *20*, 31.

[10] B. BOUKAMP, *Solid State Ion* 1986, *18–19*, 136.

[11] A. L. Gavrilyuk, D. A. Osinkin, D. I. Bronin, *Russian Journal of Electrochemistry* 2017, *53*, 575.

[12] F. Ciucci, C. Chen, *Electrochim Acta* 2015, *167*, 439.

[13] A. García, N. Papior, A. Akhtar, E. Artacho, V. Blum, E. Bosoni, P. Brandimarte, M. Brandbyge, J. I. Cerdá, F. Corsetti, R. Cuadrado, V. Dikan, J. Ferrer, J. Gale, P. García-Fernández, V. M. García-Suárez, S. García, G. Huhs, S. Illera, R. Korytár, P. Koval, I. Lebedeva, L. Lin, P. López-Tarifa, S. G. Mayo, S. Mohr, P. Ordejón, A. Postnikov, Y. Pouillon, M. Pruneda, R. Robles, D. Sánchez-Portal, J. M. Soler, R. Ullah, V. W. Z. Yu, J. Junquera, *Journal of Chemical Physics* 2020, *152*, DOI 10.1063/5.0005077.

[14] J. M. Soler, E. Artacho, J. D. Gale, A. García, J. Junquera, P. Ordejón, D. Sánchez-Portal, *Journal of Physics Condensed Matter* 2002, *14*, DOI 10.1088/0953-8984/14/11/302.

[15] S. Grimme, J. Antony, S. Ehrlich, H. Krieg, *Journal of Chemical Physics* 2010, *132*, DOI 10.1063/1.3382344.

[16] J. P. Perdew, K. Burke, M. Ernzerhof, *Phys Rev Lett* 1996, *77*, DOI 10.1103/PhysRevLett.77.3865.

[17] C. Peng, G. H. Ning, J. Su, G. Zhong, W. Tang, B. Tian, C. Su, Di. Yu, L. Zu, J. Yang, M. F. Ng, Y. S. Hu, Y. Yang, M. Armand, K. P. Loh, *Nat Energy* 2017, *2*, DOI 10.1038/nenergy.2017.74.

[18] R. P. Fornari, P. de Silva, *Wiley Interdiscip Rev Comput Mol Sci* 2021, *11*, DOI 10.1002/wcms.1495.

[19] J. Otegi, J. Carrasco, H. Manzano, 2025, DOI 10.22541/au.175258942.20206179/v1.

[20] L. Martinez, R. Andrade, E. G. Birgin, J. M. Martínez, *J Comput Chem* 2009, *30*, DOI 10.1002/jcc.21224.

[21] A. P. Thompson, H. M. Aktulga, R. Berger, D. S. Bolintineanu, W. M. Brown, P. S. Crozier, P. J. in 't Veld, A. Kohlmeyer, S. G. Moore, T. D. Nguyen, R. Shan, M. J. Stevens, J. Tranchida, C. Trott, S. J. Plimpton, *Comput Phys Commun* 2022, *271*, DOI 10.1016/j.cpc.2021.108171.

[22] W. L. Jorgensen, D. S. Maxwell, J. Tirado-Rives, *J Am Chem Soc* 1996, *118*, DOI 10.1021/ja9621760.

[23] I. V. Leontyev, A. A. Stuchebrukhov, *Journal of Chemical Physics* 2009, *130*, DOI 10.1063/1.3060164.

[24] L. S. Dodda, I. C. De Vaca, J. Tirado-Rives, W. L. Jorgensen, *Nucleic Acids Res* 2017, *45*, DOI 10.1093/nar/gkx312.

[25] N. Michaud-Agrawal, E. J. Denning, T. B. Woolf, O. Beckstein, *J Comput Chem* 2011, *32*, DOI 10.1002/jcc.21787.

[26] L. Cheng, X. Yan, J. Yu, X. Zhang, H. G. Wang, F. Cui, Y. Wang, *Advanced Materials* 2025, *37*, DOI 10.1002/adma.202411625.

[27] D. Cavaliere, A. Ikezawa, T. Okajima, H. Arai, *J Power Sources* 2024, *621*, DOI 10.1016/j.jpowsour.2024.235316.

[28] J. J. Giner-Sanz, E. M. Ortega, V. Pérez-Herranz, *J Electrochem Soc* 2018, *165*, DOI 10.1149/2.1021810jes.

[29] B. A. Boukamp, *Solid State Ion* 1986, *20*, DOI 10.1016/0167-2738(86)90031-7.

[30] B. A. Boukamp, *Solid State Ion* 1986, *18–19*, DOI 10.1016/0167-2738(86)90100-1.

[31] J. Wang, Q. A. Huang, W. Li, J. Wang, Y. Bai, Y. Zhao, X. Li, J. Zhang, *Journal of Electroanalytical Chemistry* 2022, *910*, DOI 10.1016/j.jelechem.2022.116176.

[32] Y. X. Yao, J. Wan, N. Y. Liang, C. Yan, R. Wen, Q. Zhang, *J Am Chem Soc* 2023, *145*, DOI 10.1021/jacs.2c13878.

[33] T. H. Wan, M. Saccoccio, C. Chen, F. Ciucci, *Electrochim Acta* 2015, *184*, DOI 10.1016/j.electacta.2015.09.097.

[34] H. S. Magar, R. Y. A. Hassan, A. Mulchandani, *Sensors* 2021, *21*, DOI 10.3390/s21196578.